This is a preprint, the final version is subject to change, of the American Mineralogist (MSA)
Cite as Authors (Year) Title. American Mineralogist, in press.
DOI: https://doi.org/10.2138/am-2018-6441

1

Revision 1

The effect of disequilibrium crystallization on Nb-Ta fractionation in pegmatites: constraints from crystallization experiments of tantalite-tapiolite

running title: disequilibrium crystallization in pegmatites

Marieke Van Lichtervelde[1], Francois Holtz[2] and Frank Melcher[3,4]

[1]Géosciences Environnement Toulouse, Université de Toulouse, CNES, CNRS, IRD, UPS, 31400 Toulouse, France. E-mail: marieke.vanlichtervelde@get.omp.eu

[2]Leibniz Universität Hannover, Institute of Mineralogy, 30167 Hannover, Germany

[3]Montanuniversität Leoben, 8700 Leoben, Austria

[4]Federal Institute for Geosciences and Natural Resources (BGR), 30655 Hannover, Germany

This is a preprint, the final version is subject to change, of the American Mineralogist (MSA)
Cite as Authors (Year) Title. American Mineralogist, in press.
DOI: https://doi.org/10.2138/am-2018-6441

Abstract

Tapiolite [$FeTa_2O_6$] and columbite-group minerals [$(Fe,Mn)(Ta,Nb)_2O_6$] are common Nb-Ta-bearing accessory minerals in rare-element granites and pegmatites. Their compositional gap has inspired a number of experimental studies but none of them have succeeded in reproducing the parameters that influence the gap limits. In this study, tapiolite and columbite-group minerals (CGM) were crystallized from water-saturated, flux-rich granitic melts at various conditions of pressure, temperature, oxygen fugacity and Ti contents. Crystals with a size as small as 500 nm were analyzed with a Field-Emission Gun (FEG) electron microprobe. The results show that temperature, pressure and Ti content only slightly affect the compositional gap limits between tapiolite and CGM, whereas high fO_2 leads to complete solid solution between a rutile-structured component $Fe^{3+}TaO_4$ and $(Fe,Mn)Ta_2O_6$. The experimental CGM-tapiolite gap limits are compared with natural CGM-tapiolite pairs from rare-element granites and pegmatites worldwide. This study reveals that the crystallographic structure of tapiolite and CGM could be the dominant parameter that influences the position of the compositional gap. Order-disorder in CGM and tapiolite is tightly linked to disequilibrium crystallization triggered by supersaturation. Significant isothermal Nb-Ta fractionation is observed inside CGM crystals that grow at high degrees of supersaturation. The effect of supersaturation prevails over the solubility effect that is known to increase the Ta/(Ta+Nb) ratio in CGM and coexisting melts. Thus, even if global equilibrium in terms of the solubility of Nb-Ta-bearing minerals is attained, the Ta/(Nb+Ta) ratio in the crystals may differ significantly from equilibrium. It implies that Nb-Ta fractionation in Nb-Ta oxides is controlled by crystallization kinetics rather than equilibrium chemical fractionation (or any other processes such as F-complexing of Ta or fluid exsolution) in dynamic systems which can rapidly reach supersaturated conditions. These results have important

implications for the understanding of crystallization processes in highly evolved and pegmatite-forming magmas.

Key words: crystallization experiments; disequilibrium crystallization; Nb/Ta fractionation; pegmatites; tapiolite

Introduction

Granitic pegmatites are sources of several strategic rare metals (e.g., Be, Li and Ta) which have been classified as critical based on their economic importance and supply risk (Linnen et al. 2012). As these elements are generally incompatible and poorly mobilized by hydrothermal processes, their concentration mechanisms are controlled by extreme magmatic processes that involve low degrees of partial melting of pre-enriched sedimentary rocks and extreme fractional crystallization of fertile granites. Granitic pegmatites owe their spectacular textural features (e.g., giant crystal size) and geochemical signatures (e.g., extreme fractionation of the high-field strength elements) to particular crystallization kinetics that prevail in pegmatite-forming melts at strong undercooling (London 2014a-b). The fast crystal growth in high disequilibrium leads to boundary layer formation and/or melt-melt immiscibility, two mechanisms that are reviewed in recent partly controversial papers (London 2014b; Thomas and Davidson 2014; London 2015). In addition to undercooling, the fast growth processes in pegmatite formation are enhanced by the presence of flux components such as fluorine (F), boron (B) and phosphorus (P) which considerably shift the pegmatitic melt properties toward those of an aqueous fluid, sharply depressing solidus temperature (Jahns and Burnham 1969), viscosities (Bartels et al. 2013, 2015) and crystal nucleation rates (London et al. 1989). The presence of fluxes also results in an increase of the solubilities of high-field strength element (HFSE)-bearing minerals (Linnen and Cuney 2005; Bartels et al. 2010; Aseri et al. 2015). The main problem related to HFSE-bearing mineral saturation in granitic pegmatites is that experimentally determined solubilities indicate HFSE saturation values in pegmatitic melts much higher than the concentrations determined in natural rocks. As an example, manganocolumbite and manganotantalite solubilities in water-saturated peraluminous granitic melt at 200 MPa and 800ºC (Linnen and Keppler 1997) give Nb

and Ta saturation values of ~0.2 and 0.8 wt%, respectively, which, extrapolated to conditions of pegmatite crystallization (~600ºC), correspond to saturation values of ~400 ppm Nb and 2000 ppm Ta (Linnen and Cuney 2005). However, where whole-rock compositions of rare-element pegmatites can be measured, the Nb-Ta-bearing zones display Nb and Ta concentrations in the order of tens of ppm for Nb and hundreds of ppm for Ta (e.g., Stilling et al. 2006 for the Tanco pegmatite), which is below saturation values for columbite and tantalite. Supercooling is thus invoked to explain local saturation in these minerals.

This paper presents an experimental investigation of the distribution of Nb and Ta between tapiolite and columbite-group minerals and focusses on the crystallization conditions of this common Nb-Ta mineral association. The columbite-group minerals $(Fe^{2+},Mn)(Nb,Ta)_2O_6$ consist of a solid solution between three orthorhombic end-members columbite-(Fe) $FeNb_2O_6$, columbite-(Mn) $MnNb_2O_6$, and tantalite-(Mn) $MnTa_2O_6$. Minerals of the tapiolite series are less common and mostly occur in rare-element granites and pegmatites which display a high degree of fractionation. The compositional field of the columbite-group minerals (CGM) is separated via a compositional gap from tetragonal tapiolite, whose end-member is $FeTa_2O_6$. Columbite-group minerals, especially tantalite-(Mn), and tapiolite are commonly associated in highly-fractionated rare-element granites and pegmatites (Černý et al. 1989; Wang et al. 1997; Novàk et al. 2000; Van Lichtervelde et al. 2007; Beurlen et al. 2008; Melcher et al. 2015, 2016). The chemistry and structure of tapiolite have been thoroughly investigated in the past (Clark and Fejer 1978; Lahti et al. 1983; Wise and Černý 1996; Zema et al. 2006; Ercit 2010). Černý et al. (1992) compiled a number of tapiolite-tantalite pairs from granitic pegmatites in order to establish empirically the compositional gap between the two mineral types. The extent of the compositional gap between tapiolite and CGM was experimentally studied by Moreau and Tramasure (1965), Turnock (1966), Komkov and Dubik (1974a-b), Tokizaki et al. (1986) and Tanaka et al. (1988) (see data

compilation in Černý et al. 1992). However, these experiments were conducted at conditions which are not representative of natural systems (e.g., dry conditions, elevated temperatures, atmospheric pressure). Černý et al. (1992) showed that experimental results contradict each other, especially concerning the effect of temperature on the compositional gap. The effect of impurities was not investigated, although ferric iron, Ti and Sn can reach elevated concentrations in CGM and especially in tapiolite (Wise and Černý 1996; Melcher et al. 2015, 2016).

Our study provides results on the influence of pressure, temperature, fO_2 and minor element (Ti) composition on the evolution of the compositional gap between tapiolite and CGM in nearly water-saturated melts. The melt composition was chosen to be close to the supposed composition of pegmatitic melts from which Ta-rich zones of LCT-type pegmatites form, i.e., slightly peraluminous and highly enriched in flux elements H_2O, F, Li and P, so that the experimental results can be compared to natural occurrences. However, the goal of this study was also to increase crystallization kinetics by using highly-fluxed melts in order to test the effects of kinetic parameters on the compositional gap. The results confirm that disequilibrium crystallization associated with supersaturation play a major role on the CGM-tapiolite compositional gap. The experimental results are compared with a compilation of CGM-tapiolite pairs from recent studies where the relationship between the two phases was described. This compilation is complemented by the coltan fingerprinting database of the German Federal Institute for Geosciences and Natural Resources (BGR).

Experimental procedure and analytical methods

In this study, columbite-group minerals are mostly Ta over Nb dominant, consequently for simplicity, we use the term tantalite instead of CGM in the following text. The Mn/(Mn+Fe) and Ta/(Ta+Nb) atomic ratios are hereafter referred to as Mn* and Ta*. Tantalite and tapiolite

(associated or not) were crystallized from a highly-fluxed, nearly water-saturated melt at 50 and 200 MPa and 800 to 1000ºC. The anhydrous starting glass used to produce that melt corresponds to "glass B" used by Van Lichtervelde et al. (2010) for dissolution experiments of zircon and tantalite-(Mn). Its composition is 66.9 wt% SiO_2, 16.6 wt% Al_2O_3, 3.1 wt% Na_2O, 5.7 wt% K_2O, 0.9 wt% Li_2O, 3.6 wt% P_2O_5 and 3 wt% F (Table 1). The high Li, P and F concentrations were not chosen to be representative of natural melts but instead to increase reaction kinetics in crystallization experiments. The glass has an ASI = Al/[Na+K] and an ASI_{Li} = Al/[Na+K+Li] (atomic ratios) of 1.48 and 1.16 respectively. Four other glasses were prepared with the same base composition and were doped with FeO, MnO, Ta_2O_5 and Nb_2O_5 in stoichiometric amounts of the three CGM end-members and tapiolite. An additional glass was doped with TiO_2. All glasses were prepared by mixing reagent grade oxides and carbonates (high purity SiO_2, Al_2O_3, Na_2CO_3, K_2CO_3, Li_2CO_3, AlF_3, $[NH_4]H_2PO_4$, TiO_2, MnO, FeO, Nb_2O_5 and Ta_2O_5), then finely ground in agate mortars, and melted for 2h at 1600°C and atmospheric pressure. Such high temperature inevitably provoked the loss of some lithium and fluorine but it permitted to obtain relatively homogeneous glasses without a second melting process. Starting glasses were subsequently analyzed by electron probe microanalyses (EPMA), using 15 keV, 4–6 nA, 20 µm defocused beam, 10–20 s counting times, PAP matrix correction, and standards albite, wollastonite, Al_2O_3, orthoclase, SrF_2, apatite, $MnTiO_3$, Fe_2O_3, and Ta and Nb metals. Glass compositions are reported in Table 1. Such highly-fluxed glasses are known to dissolve 6 to 10 wt% H_2O at our experimental conditions (Van Lichtervelde et al. 2010).

Starting experimental glasses with varying Mn* and Ta* were produced by mixing various proportions of the undoped glass and the four doped glass powders in order to obtain various concentrations of the doping elements (Table 2). For example, the Ta concentration necessary for tantalite saturation in our glass at 800°C and 200 MPa is around 1.3 wt% Ta_2O_5 as

134 determined by Van Lichtervelde et al. (2010). At 1000°C, this concentration is ~3.6 wt% Ta_2O_5.
135 Consequently, a glass containing 3.6 wt% Ta_2O_5 at 800°C will be supersaturated by ~280% of the
136 saturation value, or supercooled by 200°C with respect to the tantalite liquidus. Three Nb-bearing
137 experiments were doped with 0.15 wt% TiO_2. The glass powders were ground to <100 μm grain
138 size, and 30 to 40 mg of that powder was loaded with approximately 10 wt% distilled water into
139 gold capsules (15 mm long, 2.8 mm i.d., 3.0 mm o.d.). The capsules were then welded shut and
140 checked for weight loss at all stages of their preparation. Finally, closed capsules were left for at
141 least 15 min at 110°C to check for leaks before their use in experiments. Table 2 gives theoretical
142 starting glass concentrations of doping elements for each experiment, as the mixture could not be
143 analyzed prior to experiment. In order to check the starting glass compositions, three experiments
144 at 800°C were heated at 1000°C in internally heated pressure vessels (IHPV) and the
145 homogeneous glasses displayed EPMA concentrations similar to the calculated values.
146 Experiments at 800°C were conducted in water-pressurized cold-seal pressure vessels
147 (CSPV) for 12 to 14 days at 200 MPa, and quenched isobarically in a stream of air. The time
148 necessary to attain 300°C, which is the estimated glass transition temperature for hydrous granitic
149 melts was approximately 3 to 5 minutes. Several runs were conducted at 700°C, but the small
150 crystal size, coupled with slow diffusion kinetics, led to unreliable results, reflected in particular
151 by strong compositional heterogeneities in both glass and crystals. Experiments at 900°C and
152 1000°C were performed in IHPV for 5 to 8 days at 200 MPa and quenched within a few seconds
153 (Berndt et al. 2002). The fO_2 conditions in CSPV pressurized with water were close to the Ni-
154 NiO solid buffer (NNO) as imposed by the alloy of the vessel, and between NNO and NNO+1 in
155 IHPV (fO_2 controlled by the addition of H_2 to the Ar pressure medium; Berndt et al. 2002). Three
156 experiments (S6, Nb8 and Nb10; Table 2) at 800°C and 200 MPa were repeated in CSPV
157 pressurized with argon, at fO_2 conditions close to NNO+3, in order to investigate the tantalite-

158 tapiolite pairs in more oxidizing environment. One experiment (DBR), aimed at testing reaction
159 kinetics over a relatively short time, was conducted with a pure homogeneous natural tantalite-
160 (Mn) placed in a Nb- and Fe-doped glass during 3 days at 200 MPa and 800°C. For all
161 experiments run in CSPV, a multi-layer carbon foil was used to wrap the capsules to isolate them
162 from the Ni-bearing vessel. The capsules were weighed after quenching to check for leaks.
163 Several slices of experimental products were cut directly in the capsule and mounted in polished
164 sections. Experimental products, glasses and crystals, were checked for compositional
165 homogeneity by backscattered electron imaging. We carefully checked for the possible presence
166 of additional mineral phases other than CGM or tapiolite (e.g., quench phases).
167 At 900 and 1000°C, the experiments were heated slightly above the liquidus temperature
168 for tapiolite and tantalite (known from the solubility data obtained with the same glass by Van
169 Lichtervelde et al. 2010, and estimating that tapiolite and tantalite have similar solubility
170 products) during one day, and brought down 50°C below the liquidus temperature with a rapid
171 ramp (about one hour). This procedure permitted to control the undercooling degree of the
172 experiments, because undercooling by > 100°C yielded numerous very small crystals (<1µm),
173 making reliable analyses of both glass and crystals with standard EPMA difficult. The
174 experiments at 800°C were directly heated to this temperature since the CSPV could not operate
175 far above that temperature. Strong undercooling (>100°C) lead to the formation of submicron
176 crystals, but that problem could be overcome by the use of the FEG instruments for imaging and
177 analyses. For 3 experiments at 50 MPa (Nb11, 12 and 13), the temperature was first maintained at
178 500°C for three days prior to the 14-days run at 800°C, in order to avoid brutal capsule expansion
179 because of the high water contents in the capsule. Experimental conditions are summarized in
180 Table 2.
181 The experimental glasses were analyzed by EPMA (Cameca SX100, Leibniz Universität

Hannover) with the same conditions as the starting glasses for major elements (see above). For Fe, Mn, Nb, Ta and Ti, beam size was decreased to 5 μm and at the lowest Fe and Mn concentrations, counting time on the peak position was increased up to 120 s. The minimum detection limits for the lowest concentrations were around 250 ppm Mn, 270 ppm Fe, 600 ppm Ta and 550 ppm Nb at 15 keV, 20 nA and 5 μm beam size. An offline correction was applied to Ta concentrations to deal with the Si interference on Ta.

The crystalline products at 900 and 1000°C were analyzed with conventional EPMA using 15 keV, 20 nA and 10 s counting times. Those at 800°C were analyzed by Field Emission Gun EPMA (Cameca SXFive-FE, Université de Toulouse). Calculated excitation volumes in our crystals using Montecarlo simulations are 400 nm wide and 250 nm deep, using instrumental conditions of 7 keV and 40 nA. Standards are the same as for glass, i.e., Ta and Nb metals, $MnTiO_3$ and Fe_2O_3. In the absence of proper Nb-Ta standards for EPMA, pure synthetic tantalite-(Mn) was also used as secondary standard to check the quality of the Ta analyses. Structural formulae were calculated based on the AB_2O_6 composition where the A site hosts Fe+Mn and the B site hosts Nb+Ta. In the three experiments at NNO+3, ferric iron was introduced into A site by converting as much Fe^{2+} to Fe^{3+} as required to eliminate the cation excess above a total of ~3 apfu. The highest apfu totals at NNO conditions attain 3.15 apfu, which can be ascribed to small amounts of Fe^{3+} that can be present in hydrous granitic melts at NNO (Moore et al. 1995). Therefore we chose a value of 3.15 apfu as the maximum limit above which significant amounts of Fe^{3+} are present in oxidized experiments. A selection of experimental products was additionally characterized by X-ray powder diffraction in order to check the nature of crystalline products.

The small-scale characterization of crystalline products was investigated further by transmitted electron microscopy (TEM). One thin foil (15 × 10 × 0.1 μm) was cut by the FIB

technique through run Nb12 using a dual-beam FEI Helios NanoLab600i at the Université de Toulouse. TEM, SAED and STEM were performed using a JEOL cold-FEG JEM-ARM200F operated at 200kV equipped with a probe Cs corrector. EDX spectra were recorded on a JEOL CENTURIO SDD detector.

For comparison of the composition of experimental tantalite-tapiolite with natural data, we compiled data from Abella et al. (1995), Wang et al. (1997), Anderson et al. (1998), Tindle and Breaks (2000), Novàk et al. (2000, 2003), Yang et al. (2003), Selway et al. (2005), Van Lichtervelde et al. (2007), Chudik et al. (2008), Neiva et al. (2008), Küster et al. (2009), Llorens and Moro (2010), in addition to the data compilation of Černý et al. (1992). We also used the coltan fingerprinting geochemical database developed by Melcher et al. (2015; 2016). Twenty-four localities were selected and more than 2,000 analyses of coexisting CGM and tapiolite were available from rare-element granites (Nigeria) and beryl-columbite to complex spodumene subtype pegmatites in Central Africa (RDC and Rwanda). A careful sorting of the analyses was completed using backscattered electron (BSE) images of the database in order to check the cogenetic nature of the CGM-tapiolite pairs.

Results

Experimental products

All experimental products consist of homogeneous glass and tantalite and/or tapiolite crystals, except for the 3 Ti-bearing experiments which have heterogeneous Ti distribution in glasses and small (<100 nm) undefined bright particles in BSE images. The Ta, Nb, Ti, Fe and Mn concentrations in glasses are reported in Table 3. Standard deviation on the analytical set is close to the analytical uncertainty from counting statistics on each element, which is good evidence of homogeneous distribution of the doping elements. FeO, MnO, Ta_2O_5 and Nb_2O_5 concentrations in the glass were used to calculate CGM solubility products ([FeO*MnO]*[Nb_2O_5*Ta_2O_5] in

230 mol^2/kg^2) for each run following the method of Linnen and Keppler (1997). These calculations
231 are approximate as they imply ideal mixing of the four end-members and constant activity
232 coefficients. However, Figure 1 shows that the melt *to* crystals Mn* ratios are close to the ideal
233 1:1 linear correlation, so it is reasonable to assume that the activity coefficients are constant for
234 these two reactant elements, i.e., Henry's law is obeyed and concentrations can be used instead of
235 activities. Solubility products are plotted against Mn* in Figure 2.
236 The crystal size varies from <1 μm at 800°C up to 20 μm at 1000°C. If tantalite and
237 tapiolite are coexisting in one experiment, they occur as distinct grains (i.e., they are not
238 intergrown). Tapiolite is usually smaller than tantalite and displays lozenge shape whereas
239 tantalite is more tabular (Fig. 3). Chemical composition and structural formulae of the Nb-Ta-
240 bearing oxides are reported in Table 4. Within a single experiment, all crystals display a uniform
241 composition and the standard deviation on Mn* and Ta* is generally <0.05. If the size of
242 tantalite/tapiolite crystals was sufficiently large (~ 20 μm), several analyses were performed on
243 the same crystal, and the composition was found to be homogeneous. Exceptions are runs Nb11,
244 Nb12, Nb13, Nb17 and Nb19 showing Nb-rich zones in tantalite (i.e., columbite) and/or Ta-rich
245 zones in tapiolite, which is reflected by strong Ta* variations in the crystals (Figs. 3 and 4). In
246 tapiolite, the zoning pattern resembles that of sector zoning, caused by preferential bonding of Ta
247 or Nb depending on the growth faces. However, in tantalite, the low-Ta* cores surrounded by
248 high-Ta* rims rather indicate a progressive zoning (Fig. 4a). TEM results using a FIB cut through
249 run Nb12 confirm that the Nb-rich cores in tantalite are columbite (Fig. 4b). They also reveal that
250 the Nb-rich cores are oscillatory zoned (Fig. 4c). Diffraction figures were attempted on the two
251 zones in order to calculate a-c unit-cell parameters and to check order-disorder but they gave no
252 result because of the low number of exploitable oriented crystals in the foil.

In run DBR, the natural tantalite crystal reacted by dissolution-reprecipitation all along its contact with the glass, over a ~1 μm width (Fig. 5). The reaction rim forms a dark overgrowth with sharp but irregular contact with the original tantalite, and euhedral crystal shapes at the contact with the glass. Newly formed euhedral crystals of ca. 1 μm size are also present. The overgrowth and the newly-formed crystals correspond to tantalite with very homogeneous low-Ta* (i.e., columbite) composition (Fig. 5). A few points also plot in the tapiolite field, and correspond to slightly darker areas on the natural tantalite rims. Following that observation, the homogeneity of the starting tantalite was carefully checked by BSE imaging, but no tapiolite was observed. Therefore, the two new mineral phases are interpreted to represent stable products formed from the reaction between the initially Mn-Ta-rich crystal and the Fe-Nb-rich melt. The surrounding glass is homogeneous at a 5 μm scale and no diffusion profile was observed.

Structural formulae calculated on 6 oxygens display stoichiometric compositions, if we consider that the 0.1 variation around ideal site occupancy is due to errors on EPMA measurements (Table 4). Two experiments at high fO_2 (Nb8b and Nb10b) display non stoichiometric compositions, with 1.25 and 1.40 *apfu* in A site and 1.87 and 1.75 *apfu* in B site, respectively. These are the two experiments where Fe^{3+} was added into A site in order to keep the total apfu content below 3.15. Non-stoichiometry can be explained by the transition from $Fe^{2+}(Ta,Nb)_2O_6$ to $Fe^{3+}(Ta,Nb)O_4$ structures. If calculated on a 12 oxygens basis, a tapiolite composition varies between the two end members $Fe^{2+}{}_2Ta_4O_{12}$ and $Fe^{3+}{}_3Ta_3O_{12}$, where the A site varies from 2 to 3 *apfu* and the B site from 3 to 4 *apfu*. The $A^{3+}BO_4$ structure can be ascribed to a rutile structure (Wise and Černý 1996). In Ti-bearing experiments, 1/3 Ti was attributed to A site and 2/3 to B site following the substitution reaction 3 $Ti^{4+} = 2(Nb,Ta)^{5+} + (Fe,Mn)^{2+}$. Figure 6 shows that Ti is incorporated in tantalite and tapiolite along the solid solution join between $(Fe,Mn)(Nb,Ta)_2O_6$ and TiO_2, as previously shown by Linnen and Keppler (1997). It is

277 interesting to note that tapiolite hosts more Ti than tantalite in experiment Nb14, which is
278 consistent with natural tantalite-tapiolite pairs. The mechanisms of Ti partitioning between the
279 two minerals remain to be understood.

280 **Experimental limits of the compositional gap**

281 All experimental products are reported in the columbite quadrilateral in Figure 7. At 200 MPa
282 and Ta*=1, the gap extends between 0.55<Mn*<0.90 at 800°C and 0.66<Mn*<0.86 at 1000°C.
283 However, this temperature effect on the compositional gap is not observed for Nb-bearing
284 systems. At 800°C, the 3 Ti- and Nb-bearing experiments display a gap with similar limits as the
285 Ti-free experiments. At 50 MPa, the gap limit is slightly modified compared to 200 MPa, but
286 only on the tantalite side. At fO_2 conditions around NNO+3, there is no clear evidence for a
287 compositional gap and Mn* ratios of the crystals are disseminated through the whole columbite
288 quadrilateral between true tapiolite and tantalite compositions. This is explained by the presence
289 of rutile-structured $Fe^{3+}TaO_4$ crystals in addition to tapiolite and tantalite, which was verified by
290 XRD measurements in experiments Nb8b and Nb10b.

291 **Natural CGM-tapiolite pairs**

292 Figure 8 presents CGM-tapiolite compositional data for samples of the coltan fingerprinting
293 database (Melcher et al. 2015; 2016) where the two minerals are associated in one deposit. The
294 lines link the pairs that were clearly identified to be cogenetic using BSE images, as shown for
295 example in Figure 9a. The tie line extremities are located in two narrow areas that can be ascribed
296 to the compositional gap limits, delimited by the points that plot on the borders of the analytical
297 set at each locality. All localities systematically host CGM and tapiolite compositions that plot
298 inside these two bands. Moreover, many localities show extensive Nb-Ta fractionation in both

CGM and tapiolite. Tapiolite is rarely zoned, but when it is, it shows a decrease of Ta* from core to rim (Fig. 9b). To cover a dataset as complete as possible, additional data from literature published after the compilation of Černý et al. (1992) are plotted in Figure 10 and compared with the gap limits defined in Figure 8. Only two natural case studies have some Ta-Nb-bearing oxides plotting in between the compositional limits. Therefore, we consider the limits drawn in Figure 8 as representative of the whole natural dataset. The compositional limits are compared with those defined by Černý et al. (1992) in Figure 10c.

Discussion

Solubilities

Manganotantalite solubility results are comparable within error to the solubilities given by dissolution experiments with the same experimental glass (Van Lichtervelde et al. 2010), which vary from 1.3 wt% Ta_2O_5 and 0.2 wt% MnO at 800°C (log K_{sp} = -3.1), up to 3.8 wt% Ta_2O_5 and 0.6 wt% MnO at 1000°C (log K_{sp} = -2.15). The values at 800°C and 200 MPa are higher than the $MnTa_2O_6$ solubility product determined by Linnen and Keppler (1997) for peraluminous (ASI = 1.22), water-saturated granitic melt (log K_{sp} = -3.3), but similar within error to the $MnTa_2O_6$ solubility product determined by Bartels et al. (2010) for peralkaline (ASI_{Li} = 0.92), water-saturated and Li+F+B+P doped granitic melts (log K_{sp} = -2.8). The ASI_{Li} of our glass is 1.16, consequently its high flux content plays a major role in increasing solubilities, which is at least comparable to the ASI compositional effect.

The solubility products of Fe end-members as well as the Fe-Mn solid solution have never been fully investigated. Linnen and Cuney (2005) mentioned preliminary results that indicate a solubility of Fe end-members which is an order of magnitude higher compared to Mn end-members. Fiege et al. (2011) noted that the solubility of natural $(Fe,Mn)Ta_2O_6$ was higher than that of the synthetic end-members. Our results also show maximum solubilities for the

323 $(Fe,Mn)(Nb,Ta)_2O_6$ compositions close to the solid solution gap and lowest solubilities for the
324 end-members (Fig. 2). Moreover, our results show that the Mn end-members have higher
325 solubilities than the Fe end-members; this is particularly evident at 900°C, where log K_{sp}^{Mn} = -
326 2.58±0.02 and log K_{sp}^{Fe} = -2.86±0.07. These results must be considered to explain the typical Fe-
327 Mn fractionation observed in rare-element pegmatites (Van Lichtervelde et al. 2006).
328 Experiments at 200 and 50 MPa (800 °C) are useful to document the effect of pressure on
329 solubilities. The solubility product of the $(Fe,Mn)(Nb,Ta)_2O_6$ crystals is 0.3 log units lower at 50
330 MPa (log K_{sp} = -3.3) compared to 200 MPa (log K_{sp} = -3.0) (Fig. 2, Table 3), and the five points
331 obtained at 50 MPa slightly increase with increasing Mn* of the melt. Although we have no
332 solubility data for the end-member systems (melts with Mn* of 0 and 1) at this pressure,
333 extrapolation of the trend suggests that the end-members could have the same solubility products
334 at 50 and 200 MPa, since the 200 MPa data follow a curved trend with decreasing solubilities
335 toward their end-members (Fig. 2). This observation is consistent with the results of Linnen and
336 Keppler (1997) who showed that pressure has a small effect on the solubility of Mn end-
337 members. Although the solubility trends with changing Mn* need to be verified by a good
338 statistical solubility dataset, the results of Linnen and Keppler (1997) and ours are in good
339 agreement. Moreover, considering the solubility difference between $MnNb_2O_6$ and $MnTa_2O_6$
340 determined by Bartels et al. (2010) at 800°C and 200 MPa (log K_{sp}^{Nb} around -3.1 and log K_{sp}^{Ta}
341 around -2.8 for melts with Li+B+F+P totals of 7 wt%), the pressure effect on solubility observed
342 in our experiments is at least comparable to the compositional effect between columbite and
343 tantalite. In our experiments, the presence of Nb does not affect $(Fe,Mn)(Nb,Ta)_2O_6$ solubility
344 products when compared to Ta end-members (Fig. 2), likely because of the small Nb content of
345 the bulk compositions (Ta*>0.75, Table 3), except for Nb17 and Nb19.

This is a preprint, the final version is subject to change, of the American Mineralogist (MSA)
Cite as Authors (Year) Title. American Mineralogist, in press.
DOI: https://doi.org/10.2138/am-2018-6441

Experimental control on the limits of the compositional gap between tapiolite and CGM

In general, solid solutions are affected by temperature and pressure variations. In our experiments, temperature slightly affects the gap by narrowing it from 0.35 Mn* units at 800°C down to 0.20 Mn* units at 1000°C (Fig. 7). The gap limit on the tapiolite side is the most affected. This is comparable with the observation of Turnock (1966) who positioned the gap at 0.58<Mn*<0.82 at 1000°C and observed that the tantalite side of the gap was insensitive to temperature, whereas on the tapiolite side, the proportion of $MnTa_2O_6$ decreased rapidly with decreasing temperature. Turnock (1966) observed a shift on the tapiolite side from Mn* 0.70 at 1500°C to Mn* 0.58 at 1000°C, but the shift was less marked below 1000°C. Consequently, temperature does not significantly affect the gap limits at pegmatite forming temperatures, i.e., below 700°C. Pressure is found to have even lower influence on the gap. A pressure drop from 200 MPa to 50 MPa only shifts the tantalite side of the gap limit by less than 0.1 Mn* unit toward higher Mn* (Fig. 7).

The presence of Ti in Nb-bearing tantalite and tapiolite does not affect the gap limits. However, at oxidizing conditions and in systems with high $Fe^{3+} / (Fe^{3+} + Fe^{2+})$ ratio, the formation of ABO_4 phases containing Fe^{3+} (up to 40% total Fe) and with Mn* ratios plotting within the compositional gap is observed. Although there are only two experiments with coexisting tapiolite and CGM at oxidizing conditions, we note that this phase can coexist with a tantalite phase (Nb10b, Table 4). Turnock (1966) showed that Fe is mostly divalent in natural tantalite whereas tapiolite can host both Fe^{2+} and Fe^{3+}, with compositions plotting on the join $FeTa_2O_6$-$FeTaO_4$, and suggested that the presence of Mn in the solid solution makes it more resistant to oxidation. This seems to be confirmed in our dataset, as the $Fe^{3+} / (Fe^{3+} + Fe^{2+})$ ratio in the solid solution decreases with increasing Mn*.

Černý et al. (1992) suggested that cation order-disorder in CGM and tapiolite could impact the mineral stabilities and therefore the position of the compositional gap. However, rare are the studies that investigate CGM and tapiolite structures together with their chemistry and crystallization history in pegmatites (Clark and Fejer 1978; Abella et al. 1995; Mulja et al. 1996; Lumpkin 1998; Novàk et al. 2000; Galliski and Černý 2006; Wise et al. 2012). Natural CGM and tapiolite generally display disordered crystal lattices, and the reason for this disordered state is poorly understood. It requires determining *in situ* the unit-cell parameters at a scale smaller than that of the complex zoning that is commonly observed in these minerals. Cation order-disorder is reflected structurally in the a-c unit-cell parameters (Wise et al. 1985) and chemically in the A site vs. B site occupancy. Strong disorder leads to heterogeneous distribution of Fe+Mn and Nb+Ta between the two sites, i.e., minor amounts of Fe+Mn occupy the B site and minor amounts of Ta+Nb the A site, therefore leading to non-stoichiometry in the chemical formulae. Figure 11 shows A site vs. B site occupancy for our experimental products at 800°C. It shows that crystals formed at 200 MPa tend to have a better stoichiometry (i.e., A and B site occupancy is close to 1 and 2 apfu, respectively) than at 50 MPa (compare also runs S5 and T7, which are duplicate experiments at 50 and 200 MPa, in Table 4), even for Ti-bearing experiments. Experiments at NNO+3 show the highest deviation from stoichiometry with the two Fe^{3+}-bearing samples tending toward ABO_4 stoichiometry. If the degree of order-disorder can be estimated from the deviation of the apfu content of A and B sites from their ideal values of 1 and 2, respectively, then the experimental products at NNO+3 and those at 50 MPa can be considered as disordered, whereas those at 200 MPa are relatively ordered. In Figure 11, those experiments lie above 1.10 apfu in A site and below 1.95 apfu in B site. Samples plot on a linear trend with a negative slope of -2:5, which is necessary for maintaining charge balance, and the total apfu increases above 3; this is coherent with a disordering effect that tends to increase the cell volume.

This is a preprint, the final version is subject to change, of the American Mineralogist (MSA)
Cite as Authors (Year) Title. American Mineralogist, in press.
DOI: https://doi.org/10.2138/am-2018-6441

One experiment (Nb8) displays tapiolite with apfu totals of 1 and 2, respectively, for A and B sites, which can be considered as our most ordered tapiolite composition. It is interesting to note that the natural tantalite-(Mn) used as a starting product for the reverse experiment also plots in the disordered side, whereas the Nb-rich tantalite crystallization product plots in the ordered side. In conclusion, the relative values in A and B site occupancy between ideal stoichiometry and non-stoichiometry can be used as an indicator of the degree of order-disorder in the crystals. However, this indication remains speculative in the absence of unit-cell parameters determination, which was impossible from XRD data because of the small volume of our crystal products in the experiments.

There is a good correlation between the presence of Nb-Ta heterogeneities in our crystals and their disorder degree as determined from Figure 11. All runs at 50 MPa display low-Ta* zones in tantalite and/or high-Ta* zones in tapiolite, and they all plot as disordered. Run Nb19 also has tantalite plotting on the disordered side, similarly to the 50 MPa runs, and it displays one low-Ta* tantalite analysis. Consequently, these heterogeneities in the crystals are suspected to be related to crystal disorder. The minerals with Ta* which are very far from the compositional gap limits seem to be the most disordered.

In conclusion, the crystallographic structure (i.e., unit cell parameters, and in particular the order-disorder state) of tapiolite and CGM seems to be the dominant parameter that influences the position of the compositional gap. The incorporation of Fe^{3+} strongly impacts on the tapiolite structure through a complete solid solution with tetragonal, rutile-structured $[(Mn^{2+},Fe^{2+},Fe^{3+})(Ta,Nb)O_4]$, which displays no gap between Fe and Mn end-members. On the other hand, the incorporation of minor elements such as Ti does not modify tapiolite and CGM structure (Tarantino et al., 2003), and the gap is not affected either.

Comparison between experimental and natural compositional gap

Figure 12 synthesizes the compositions of our experimental phases crystallized at 800ºC which are compared with the natural gap limits as defined in Figure 8. The natural immiscibility gap for CGM is comparable to the gap determined experimentally at 200 MPa, even with the Ti-bearing runs (Fig. 12). However, the natural gap limit on the tapiolite side is considerably shifted toward lower Mn* ratios compared to the experimental gap limit. In natural assemblages, the highest Mn-bearing tapiolite has a Ta* ratio close to 1 and accommodates Mn* ratios up to 0.33 (Bikita pegmatite, Zimbabwe, Černý et al. 1992). In our experiments, tapiolite at Ta*=1 reaches Mn* of 0.55. This value may be slightly shifted toward lower Mn* around 0.45 if we extrapolate the limits at 500ºC, which is a reasonable temperature for tapiolite crystallization in the most highly-fractionated pegmatites. Pressure and Ti probably do not significantly influence the position of the gap and the presence of Fe^{3+} tends to decrease the width of the compositional gap. The lack of correspondence in Mn* of natural and experimental tapiolite could indicate a poor correlation of our experiments with natural settings. However, if we presume that the negligible dependence on temperature from our experiments is accurate, and the conditions of our experiments apply to natural occurrences, then other processes must be invoked to explain the shift of the natural tapiolite gap limit toward lower Mn*.

The effect of disequilibrium crystallization

All 50 MPa experiments show significant Nb-Ta heterogeneities in the form of either low-Ta* zones in tantalite or high-Ta* zones in tapiolite or both. Such heterogeneities are not observed at 200 MPa, except for one low-Ta* point of Nb19. Tantalite and tapiolite compositions are even more homogeneous in 1000°C runs. Nb-Ta heterogeneities occur both in isothermal (Nb10 and Nb17, 800°C) and two-stage (Nb11, Nb12 and Nb13, 500 → 800°C) experiments. Therefore, the

3-days step at 500°C cannot have caused this heterogeneity.

TEM images show that the low-Ta* (i.e., columbite) cores in tantalite can be oscillatory-zoned. This characteristic feature of CGM is commonly interpreted as fast crystallization in disequilibrium from the melt (Van Lichtervelde et al. 2007). Disequilibrium crystallization leads to high strain in the crystal lattice, favoring entrance of the most compatible element (Morgan and London 2003). In the meantime, supersaturation (i.e., concentration values in the melt much higher than the concentrations required for saturation in a mineral phase) is also expected to have an effect on the composition of CGM. At strong supersaturation, the crystal growth rate is fast (once nucleation has occurred) and the composition of the mineral at the interface with melt is dependent on diffusion kinetics in the melt phase (London 2014b). The impact of supersaturation is expected to be pronounced for slow-diffusing cations such as Nb and Ta. If Nb and Ta diffusivities are too slow to keep a homogeneous equilibrium concentration at the crystal-melt interface, the most compatible element (Nb here) is depleted at the crystallization front, whereas the most incompatible element (Ta here) concentrates at the interface. This process was illustrated experimentally for undercooled hydrous granite systems by Morgan and London (2003) who observed Ba-rich cores in alkali feldspar formed in isothermal experiments and interpreted them as the result of far-from-equilibrium crystallization in supercooled conditions. In our case study, Nb and Ta are major constituents in CGM, and the crystallization of CGM is controlled by solubility laws. Since Linnen and Keppler (1997) showed that Ta end-members are more soluble than Nb end-members, the Ta* ratio is expected to be higher in the melt than in CGM, and CGM favors Nb over Ta in its crystal lattice even though the melt contains more Ta than Nb atoms. The low-Ta* tantalite would then record high disequilibrium, and by extension, high-Ta* tapiolite as well, whereas crystal rims would record equilibrium. Negligible solid-state diffusion at the timescale and temperature of our experiments (Marschall et al. 2013), even at the nanometer

scale of the oscillatory zoning, would have allowed the zoning to be preserved after crystallization. At 50 MPa, the three mechanisms (i.e., high disequilibrium in the crystals, high supersaturation in the melt and slow lattice diffusion after crystallization) work for the formation and preservation of zoned crystals. This could explain the poor stoichiometry ascribed to high disorder in the crystal lattice at 50 MPa. However, the link between disequilibrium crystallization and order-disorder in the crystals is not obvious in the absence of structural data.

Run DBR is also initially far from equilibrium and the reaction of the natural tantalite crystal with the Fe-Nb-doped glass generated low-Ta* tantalite and high-Ta* tapiolite whose Ta* are consistent with those of disequilibrium phases in crystallization experiments. The $(Fe,Mn)(Nb,Ta)_2O_6$ solubility product is slightly lower than in the 13-days crystallization experiments, which is ascribed to the higher Nb content of that run compared to crystallization experiments. Consequently, the melt diffusion kinetics were fast enough to allow a bulk Nb+Ta re-equilibration of the melt (i.e., the solubility product is attained), but the newly-formed Nb-Ta oxides did not have time to re-equilibrate for Ta* by dissolution-reprecipitation or crystal lattice diffusion over the 3-days run duration.

Disequilibrium crystallization in our experiments can be caused by supersaturation. If we choose $[Ta_2O_5+Nb_2O_5]$ concentration in the melt as a measure of saturation, we can estimate the saturation degree from the difference in $[Ta_2O_5+Nb_2O_5]$ concentrations between the final and the starting glasses for each experiment. For experiments at 50 MPa and 800ºC, i.e., Nb11, Nb12, Nb13 and Nb17, $[Ta_2O_5+Nb_2O_5]^{start}$ is 2.5 to 2.7 wt% and $[Ta_2O_5+Nb_2O_5]^{final}$ is 0.64 to 0.74 wt%, which gives a supersaturation degree of ~ 360 to 400%. For experiments at 200 MPa and 800ºC, i.e., Nb8, Nb9, Nb10 and Nb19, $[Ta_2O_5+Nb_2O_5]^{start}$ is also 2.5 to 2.7 wt% and $[Ta_2O_5+Nb_2O_5]^{final}$ is 1 to 1.1 wt% (except Nb19 which has a lower solubility ~ 0.7 wt%), which gives a supersaturation degree of ~ 250 to 275%, except for Nb19 (350%). The experiments that have

487 supersaturation degrees >350% (Nb11, Nb12, Nb 13, Nb17 and Nb19) all display extensive Nb-
488 Ta fractionation in tantalite and/or tapiolite. Consequently, the occurrence of strong Nb-Ta
489 fractionation in our experiments can be directly correlated with their supersaturation degree. In
490 our experiments, supersaturation is stronger at 50 MPa because the $(Fe,Mn)(Nb,Ta)_2O_6$ phases
491 have 0.3 log units lower solubility products compared to 200 MPa (Fig. 2). The strong Nb-Ta
492 fractionation observed in Nb19 and in all runs at 50 MPa cannot be explained by the solubility
493 difference between Nb and Ta end-members and can only be explained by the stronger
494 supersaturation degree compared to the other runs.

495 If low-Ta* zones in tantalite or high-Ta* zones in tapiolite are considered as
496 disequilibrium phases, then a second limit can be drawn through our low-Ta* tantalite and high-
497 Ta* tapiolite compositions (dashed lines in Fig. 12). In the tapiolite field, that limit is close to the
498 limit observed from natural occurrences. In the CGM field, that limit encompasses most natural
499 CGM compositions. Consequently, CGM and tapiolite compositions that plot near the
500 compositional gap limits (plain lines of Fig. 12) can be considered as stable equilibrium phases,
501 whereas disequilibrium considerably modifies their Ta* ratios. We therefore suggest that
502 disequilibrium crystallization is critical in controlling the Ta* ratio, and therefore Nb-Ta
503 fractionation, of tapiolite and CGM. The classical evolution from columbite to tantalite observed
504 in evolved melts, such as rare-element granites and pegmatites, would then reflect disequilibrium
505 crystallization rather than differential solubility. The fact that natural tapiolite plots far from the
506 experimentally-determined limit at equilibrium suggests that natural tapiolite always crystallizes
507 at disequilibrium, which could reflect high supersaturation degrees during tapiolite
508 crystallization.

Implication for pegmatite formation and Nb-Ta fractionation

In magmatic systems supersaturation can be caused by several processes. The most important ones in fast cooling and low viscosity melts are 1) strong undercooling (supercooling), due for example to nucleation delay, and 2) loss from the melt of any component that influences phase stabilities. For example, water loss as a result of decompression and fluid exsolution is known to lead to the crystallization of solid phases. Flux elements (F, Li, B, P) other than water may also have a major effect on supersaturation. F and Li can cause a depolymerization of the melt (Bartels et al. 2015) which in turn has strong effects on nucleation and growth of mineral phases upon cooling (London 2014b). Figure 1a of London (2014b) illustrates the nucleation delay with undercooling in the haplogranite ternary system. This process can be extended to solid solutions, and the Ta* of CGM is controlled by the Gibbs Free Energy of Nb and Ta end-members. In the absence of thermodynamic data for tapiolite and CGM minerals, one can calculate theoretically the free energy change ($\Delta_fG°$) for the crystallization reaction of each CGM end-member using $\Delta_fG°$ of the pure oxides FeO, MnO, Nb_2O_5 and Ta_2O_5 (appendix). The $\Delta_fG°$ is higher for Nb end-members than for Ta end-members. Thus, the Nb end-members tend to crystallize before Ta end-members with decreasing temperature. With supersaturation, $\Delta_fG°$ decreases faster for Ta end-members than Nb end-members, so that CGM proto-crystals tend to incorporate more Nb relative to Ta compared to an equilibrium crystallization sequence. This leads to a Ta* in CGM crystals which is lower than the equilibrium value, and by consequence residual melts with Ta* higher than the equilibrium value. Thus, disequilibrium crystallization may produce fractionation trends that mimic equilibrium fractionation trends with slow cooling, but which may lead to melt Nb/Ta ratios much smaller than 1 (London 2014b, London and Morgan 2017). Wherever tapiolite is

present, Nb-Ta fractionation is always highest (Fig. 8), which suggests that Ta-rich phases require degrees of supercooling that are higher than for Nb-rich phases in order to precipitate.

Implication for Nb-Ta fractionation in flux-rich evolved melts

Extreme fractionation of the HFSE, especially those geochemical twins like Zr-Hf or Nb-Ta, that should not fractionate during any Earth processes, have been a matter of debate since Hofmann (1988) and Green (1995) noted their inconsistent behavior during oceanic and continental crust differentiation. One theory to explain strong Nb-Ta fractionation in crustal melts relies on the differential Nb-Ta partitioning in micas (the only Nb-Ta-bearing mineral with rutile in granites) during fractional crystallization (Stepanov et al. 2014). We applied the Rayleigh fractionation model of Stepanov et al. (2014) to muscovite- and rutile-bearing granite, and Nb-Ta partitioning in micas leads to melt enrichment by factors of 2 for Nb and 6 for Ta for a magma containing 10% muscovite and 0.2% rutile after 90% crystallization, which would bring the initial melt Nb/Ta ratio of 10 down to 3. In order to get Nb/Ta ratios <1 that are typical of granitic pegmatites, 99.9% crystallization of a granitic rock containing 15% muscovite and 0.2% rutile in addition to the major silicates is required. In the most evolved melts, other processes than mica fractionation can decrease the Nb/Ta ratio even more. Possible processes proposed so far are 1) the higher solubility of Ta end-members relative to Nb end-members of Nb-Ta-Ti oxides in granitic melts (Linnen and Keppler 1997), 2) the preferential complexing of Ta by fluorine in highly evolved F-Li-rich melts (Černý et al. 1986), and 3) fluid exsolution (Ballouard et al. 2016). However, the hypothesis of fluid exsolution is not confirmed by experimental results showing that Nb/Ta fractionation is in favor of Nb in F-rich fluids (Zaraiski et al. 2010), and this scenario fails to explain the strong Nb-Ta enrichment that systematically accompanies Nb/Ta ratios <1 (Ballouard et al. 2016) as the vapor-melt partition coefficients for Nb and Ta are near to

zero, even in F-rich fluids (Chevychelov et al. 2005). Further arguments against the possibility of Nb-Ta fractionation by fluid-related processes are brought by Stepanov et al. (2016).

In evolved magmatic systems, Nb-Ta-bearing oxides become the main phases controlling Nb-Ta fractionation as well as the concentrations of Nb and Ta in the residual melt. Following the solubility laws for Nb-Ta-bearing oxides, the Nb and Ta concentrations are expected to decrease with decreasing temperature. However, if the nucleation of these minerals is delayed, Nb and Ta concentrations keep increasing. After 90% crystallization, including 15% muscovite and no rutile, the Nb and Ta concentrations are enriched by 3 and 9 times, respectively, but the Nb/Ta ratio remains above 2. Thus, mica fractionation can explain Nb-Ta fractionation in peraluminous granitic melts down to Nb/Ta ratios of ~ 2 (Stepanov et al. 2014). However, further Nb-Ta fractionation leading to ratios < 1 in evolved, Li+F-bearing granitic and pegmatitic melt cannot be explained by muscovite fractionation only and also not by fluid exsolution (see Fig. 2b of Ballouard et al. 2016). On the other hand, our experimental results on Nb-Ta oxides show that the Nb/Ta ratios are highly sensitive to supersaturation with respect to these phases and the effect of disequilibrium crystallization of Nb-Ta-bearing oxides due to strong undercooling may prevail over that resulting from equilibrium crystallization and fractionation. As a consequence, at strong undercooling, the Ta/(Nb+Ta) ratio of crystallizing Nb-Ta oxides and of coexisting melts is not controlled by the equilibrium distribution of Nb and Ta between these phases. Rutile is also a common Nb-Ta-Ti-bearing accessory mineral in evolved peraluminous granites and pegmatites. Considering that its behavior is close to that of CGM in these magmatic environments (Linnen and Keppler 1997), it is probable that rutile nucleation delay and supersaturation may lead to Nb-Ta fractionation trends similar to CGM, leading to Nb/Ta ratios much smaller than 1.

Conclusion

Crystallization experiments of tapiolite and columbite-group minerals at high degrees of supersaturation reveal significant isothermal Nb-Ta fractionation that cannot be related to solubility differences. The gap limits between these two minerals are shown to be poorly influenced by temperature, pressure and Ti content, whereas supersaturation (above 350% of the saturation value) deports the gap limits away from the limits defined by CGM and tapiolite pairs at equilibrium. Supersaturation provokes disequilibrium crystallization, which impacts the Gibbs free energy change of the crystallization reaction for Nb and Ta end-members, therefore leading to the formation of Nb-rich CGM and Ta-rich tapiolite away from their equilibrium compositional range. Comparison between experimental results and natural assemblages suggests that tapiolite never crystallizes in equilibrium in rare-element granites and pegmatites, which confirms the strong disequilibrium inferred in late flux-rich melts at the origin of these rocks. Disequilibrium crystallization at strong degrees of supersaturation would produce the zoned and disordered CGM and tapiolite crystals classically observed in pegmatites. Strong undercooling (i.e., supercooling) is inferred to be a dominant mechanism in the evolution of granitic melts toward Nb-Ta-oxide saturation and extreme Nb-Ta fractionation.

Acknowledgments

This work benefited from the contribution of D. Guillaume, A. Wegorzewski and A. Stechern in running the experiments, and S. Gouy and P. de Parseval in developing FEG-EPMA procedures. We are also grateful to S. Goldmann for helping with the BGR database, J. Lodziak for EPMA analyses of natural CGM, and C. Josse, T. Hungria and L. Datas for FIB and TEM techniques. Constructive comments by D. London, J.M. Hanchar, M. Wise and A. Stepanov greatly enhanced

598 the quality of the manuscript. This work was supported by the German Research Foundation
599 (DFG project Ho 1337/20) and the French National Research Agency (ANR project VARPEG).

600 **References**

601 Abella, P.A., Cordomi, M.C., and Draper, J.-C. (1995) Nb-Ta minerals from the Cap de Creus
602 pegmatite field, eastern Pyrenees: distribution and geochemical trends. Mineralogy and
603 Petrology, 55, 53-69.
604 Anderson, A.J., Černý, P., Halden, N.M., and Uher, P. (1998) The Yitt-B pegmatite swarm at
605 Bernic Lake, southeastern Manitoba: a geochemical and paragenetic anomaly. Canadian
606 Mineralogist, 36, 283-301.
607 Aseri, A.A., Linnen, R.L., Dong Che, X., Thibault, Y., and Holtz, F. (2015) Effects of fluorine on
608 the solubilities of Nb, Ta, Zr and Hf minerals in highly fluxed water-saturated haplogranitic
609 melts. Ore Geology Reviews, 64, 736-746.
610 Ballouard, C., Poujol, M., Boulvais, P., Branquet, Y, Tartèse, R, and Vigneresse, J.-L. (2016) Nb-
611 Ta fractionation in peraluminous granites: A marker of the magmatic-hydrothermal
612 transition. Geology, 44, 231-234.
613 Bartels, A., Holtz, F., and Linnen, R.L. (2010) Solubility of manganotantalite and
614 manganocolumbite in pegmatitic melts. American Mineralogist, 95, 537-544.
615 Bartels A., Behrens, H., Holtz, F., Schmidt, B.C., Fechtelkord, M., Knipping, J., Crede, L.,
616 Baasner, A., Pukallus, N. (2013) The effect of fluorine, boron and phosphorus on the
617 viscosity of pegmatite forming melts. Chemical Geology, 346, 184-198.
618 Bartels, A., Behrens, H., Holtz, F., and Schmidt, B.C. (2015) The effect of lithium on the
619 viscosity of pegmatite forming liquids. Chemical Geology, 410, 1-11.

620 Berndt, J., Liebske, C., Holtz, F., Freise, M., Nowak, M., Ziegenbein, D., Hurkuck, W., Koepke,
621 J. (2002) A combined rapid-quench and H_2- membrane setup for internally heated pressure
622 vessels: description and application for water solubility in basaltic melts. American
623 Mineralogist, 87, 1717-1726.
624 Beurlen, H., Da Silva, M.R.R., Thomas, R., Soares, D.R., and Olivier, P. (2008) Nb–Ta–(Ti–Sn)
625 oxide mineral chemistry as tracer of rare- element granitic pegmatite fractionation in the
626 Borborema Province, Northeastern Brazil. Mineralium Deposita, 43, 207-228.
627 Černý, P., Goad, B.E., Hawthorne, F.C., and Chapman, R. (1986) Fractionation trends of the Nb-
628 and Ta-bearing oxide minerals in the Greer Lake pegmatitic granite and its pegmatite
629 aureole, southeastern Manitoba. American Mineralogist, 71, 501-517.
630 Černý, P., Chapman, R., Chackowsky, L.E., and Ercit, T.S. (1989) A ferrotantalite- ferrotapiolite
631 intergrowth from Spittal a.d. Drau, Carinthia, Austria. Mineralogy and Petrology, 41, 53-63.
632 Černý, P., Ercit, T.S., and Wise, M.A. (1992) The tantalite-tapiolite gap: natural assemblages
633 versus experimental data. Canadian Mineralogist, 30, 587-596.
634 Chevychelov, V.Y., Zaraisky, G.P., Borisovsky, S.E., and Borkov, D.A. (2005) Effect of melt
635 composition and temperature on the partitioning of Ta, Nb, Mn, and F between granitic
636 (alkaline) melt and fluorine-bearing aqueous fluid: fractionation of Ta and Nb and conditions
637 of ore formation in rare-metal granites. Petrology, 13, 305-321.
638 Chudík, ., Uher, P., Kohút, M., and Bačík, . (2008) Accessory columbite to tantalite, tapiolite
639 and zircon: products of extreme fractionation in highly peraluminous pegmatitic granite from
640 the Považš ý Inovec Mountains, Western Carpathians, Slovakia. Journal of Geosciences, 53,
641 323-334.
642 Clark, A.M., and Fejer, E.E. (1978) Tapiolite, its chemistry and cell dimensions. Mineralogical
643 Magazine, 42, 477-480.

644 Ercit, T.S. (2010) Hidden story of tapiolite. Mineralogical Magazine 74, 715-729.

645 Fiege, A., Kirchner, C., Holtz, F., Linnen, R.L., and Dziony, W. (2011) Influence of fluorine on
646 the solubility of manganotantalite ($MnTa_2O_6$) and manganocolumbite ($MnNb_2O_6$) in granitic
647 melts - An experimental study. Lithos, 122, 165-174.

648 Galliski, M.A., and Černý, P. (2006) Geochemistry and structural state of columbite-group
649 minerals in granitic pegmatites of the Pampean Ranges, Argentina. Canadian Mineralogist,
650 44, 645-666.

651 Green, T.H. (1995) Significance of Nb/Ta as an indicator of geochemical processes in the crust-
652 mantle system. Chemical Geology, 120, 347-359.

653 Hofmann, A.W. (1988) Chemical differentiation of the Earth: the relationship between mantle,
654 continental crust, and oceanic crust. Earth and Planetary Science Letters, 90, 297-314.

655 Jahns, R.H., and Burnham, C.W. (1969) Experimental studies of pegmatite genesis: I. A model
656 for the derivation and crystallization of granitic pegmatites. Economic Geology, 64, 843–
657 864.

658 Komkov, A.I., and Dubik, O.Y. (1974a) On the conditions of stability of columbite $FeNb_2O_6$ and
659 tapiolite $FeTa_2O_6$. In: Frank-Kamenetskyi, V.A. (ed) Crystal Chemistry and Structural
660 Mineralogy, 25-30.

661 Komkov, A.I., and Dubik, O.Y. (1974b) Experimental examination of polymorphic and
662 isomorphic relationships in the system $FeNb_2O_6$ – $FeTa_20_6$ - $MnTa_2O_6$ - $MnNb_2O_6$. In:
663 Frank-Kamenetskyi, V.A. (ed) Crystal Chemistry and Structural Mineralogy, 82-93.

664 Küste , D., Romer, R.L., Tolessa D., Zerihun, D., Bheemalingeswara, K., Melcher, F., and
665 Oberthür, T. (2009) The Kenticha rare-element pegmatite, Ethiopia: internal differentiation,
666 U–Pb age and Ta mineralization. Mineralium Deposita, 44, 723-750.

667 Lahti, S.I., Johanson, B., and Virkkunen (1983) Contributions to the chemistry of tapiolite-
668 manganotapiolite, a new mineral. Bulletin of the Geological Society of Finland, 55, 101-109.
669 Linnen, R.L., Van Lichtervelde, M., and Černỳ, P. (2012) Granitic pegmatites as sources of
670 strategic metals. Elements, 8, 275-280.
671 Linnen, R.L., and Keppler, H. (1997) Columbite solubility in granitic melts: Consequences for
672 the enrichment and fractionation of Nb and Ta in the Earth's crust. Contributions to
673 Mineralogy and Petrology, 128, 213–227.
674 Linnen, R.L., and Cuney, M. (2005) Granite-related rare-element deposits and experimental
675 constraints on Ta–Nb–W–Sn–Zr–Hf mineralization. In: Linnen, R.L. and Sampson, I.M.
676 (eds.) Rare-element Geochemistry and Mineral Deposits. Geological Association of Canada
677 Short Course Notes, 17, 45–68.
678 Llorens, T., and Moro, M.C. (2010) Microlite and tantalite in the LCT granitic pegmatites of La
679 Canalita, Navasfría Sn–W district, Salamanca, Spain. Canadian Mineralogist, 48, 375-390.
680 London, D. (2014a) A petrologic assessment of internal zonation in granitic pegmatites. Lithos,
681 184–187, 74–104.
682 London, D. (2014b) Subsolidus isothermal fractional crystallization. American Mineralogist, 99,
683 543-546.
684 London, D. (2015) Reply to Thomas and Davidson on "A petrologic assessment of internal
685 zonation in granitic pegmatites" (London, 2014a). Lithos, 212-215, 469-484.
686 London, D., Morgan, G.B. (2017) Experimental crystallization of the Macusani obsidian, with
687 applications to lithium-rich granitic pegmatites. Journal of Petrology, 58, 1005-1030.
688 London, D., Morgan, G. B., VI, and Hervig, R. L. (1989) Vapor-undersaturated experiments in the
689 system macusanite–H_2O at 200 MPa, and the internal differentiation of granitic pegmatites.
690 Contributions to Mineralogy and Petrology, 102, 1–17.

691 Lumpkin, G.R. (1998) Composition and structural state of columbite-tantalite from the Harding
692 pegmatite, Taos county, New Mexico. Canadian Mineralogist, 36, 339-353.
693 Marschall, H.R., Dohmen, R., Ludwig, T. (2013) Diffusion-induced fractionation of niobium and
694 tantalum during continental crust formation. Earth and Planetary Science Letters, 375, 361-
695 371.
696 Melcher, F., Graupner, T., Gäbler , H.-E., Sitnikova, M., Henjes-Kunst, F., Oberthür , T., Gerdes,
697 A., Dewaele, S. (2015) Tantalum–(niobium–tin) mineralisation in African pegmatites and
698 rare metal granites: constraints from Ta–Nb oxide mineralogy, geochemistry and U–Pb
699 geochronology. Ore Geology Reviews, 64, 667-719.
700 Melcher, F., Graupner, T., Gäbler , H.-E., Sitnikova, M, Oberthür , T., Gerdes, A., Badanina, E.,
701 Chudy, T. (2016) Mineralogical and chemical evolution of tantalum–(niobium–tin)
702 mineralisation in pegmatites and granites. Part 2: Worldwide examples (excluding Africa)
703 and an overview of global metallogenic patterns. Ore Geology Reviews (in press).
704 Moore, G., Righter, K., Carmichael. I.S.E. (1995) The effect of dissolved water on the oxidation
705 state of iron in natural silicate liquids. Contributions to Mineralogy and Petrology, 120, 170-
706 179.
707 Morgan, G.B., and London, D. (2003) Trace-element partitioning at conditions far from
708 equilibrium: Ba and Cs distributions between alkali feldspar and undercooled hydrous
709 granitic liquid at 200 MPa. Contributions to Mineralogy and Petrology, 144, 722-738.
710 Moreau, J., and Tramasure, G. (1965) Contribution à l'étude des séries columbite-tantalite et
711 tapiolite-mossite. Annales de la Société Géologique de Belgique, 88, 301-328.
712 Mulja, T., Williams-Jones, A.E., Martin, R.F., and Wood, S.A. (1996) Compositional variation
713 and structural state of columbite-tantalite in rare-element granitic pegmatites of the Preissac-
714 Lacorne batholith, Quebec, Canada. American Mineralogist, 81, 146-157.

715 Neiva, A.M.R, Gomes, M.E.P, Ramos, J.M.F., and Silva, P.B. (2008) Geochemistry of granitic
716 aplite-pegmatite sills and their minerals from Arcozelo da Serra area (Gouveia, central
717 Portugal). European Journal of Mineralogy, 20, 465-485.
718 Nova̋k, M., Uhe , P., Černý, P., and Siman, P. (2000) Compositional variations in
719 ferrotapiolite+tantalite pairs from the beryl-colombite pegmatite at Moravany nad Vahom,
720 Slovakia. Mineralogy and Petrology, 69, 295-306.
721 Nova̋k, M., Černý, ., and Uher, P. (2003) Extreme variation and apparent reversal of Nb-Ta
722 fractionation in columbite-group minerals from the Scheibengraben beryl-columbite granitic
723 pegmatite, Marsikov, Czech Republic. European Journal of Mineralogy, 15, 565-574.
724 Selway, J.B., Breaks, F.W., and Tindle, A.G. (2005) A Review of Rare-Element (Li-Cs-Ta)
725 Pegmatite Exploration Techniques for the Superior Province, Canada, and Large Worldwide
726 Tantalum Deposits. Exploration and Mining Geology, 14, 1-30.
727 Stepanov, A., Mavrogenes, J.A., Meffre, S., and Davidson, P. (2014) The key role of mica during
728 igneous concentration of tantalum. Contributions to Mineralogy and Petrology, 167, 1–8.
729 Stepanov, A., Meffre, S., Mavrogenes, J, and Steadman, J. (2016) Comment to “Nb-Ta
730 fractionation in peraluminous granites: A marker of the magmatic-hydrothermal transition”
731 by Ballouard et al. (2016). Geology Forum, e394.
732 Stilling, A., Černý, P., and Vanstone, P.J. (2006) The Tanco pegmatite at Bernic Lake, Manitoba.
733 XVI. Zonal and bulk compositions and their petrogenetic significance. Canadian
734 Mineralogist, 44, 599–623.
735 Tanaka, I., Inoue, R., and Kojima, H. (1988) Single crystal growth of tantalite
736 ($(Fe,Mn)(Ta,Nb)_2O_6$) solid solutions. Journal of Crystal Growth, 91, 141-146.
737 Tarantino, S.C., Zema, M., Pistorino, M., and Domeneghetti, C. (2003) High-temperature X-ray
738 investigation of natural columbites. Physics and Chemistry of Minerals, 30, 590-598.

739 Thomas, R., and Davidson, P. (2014) Comment on "A petrologic assessment of internal zonation
740 in granitic pegmatites" by David London (2014). Lithos, 212-215, 462-468.
741 Tindle, A.G., and Breaks, F.W. (2000) Columbite-tantalite mineral chemistry from rare- element
742 granitic pegmatites: Separation Lake area, N.W. Ontario, Canada. Mineralogy and Petrology,
743 70, 165-198.
744 Tokizaki, E., Sugitani, Y., and Nagashima, K. (1986). Phase diagram and valence state of iron in
745 $FeNb_2O_6$ synthesized under controlled redox atmosphere. Materials Research Bulletin 21,
746 231-236.
747 Turnock, A.C. (1966) Synthetic wodginite, tapiolite and tantalite. Canadian Mineralogist, 8, 461-
748 470.
749 Van Lichtervelde, M., Linnen, R.L., Salvi, S., and Beziat, D. (2006) Evaluating the role of
750 metagabbro rafts on tantalum mineralisation in the Tanco pegmatite, Manitoba. Canadian
751 Mineralogist, 44, 625-644.
752 Van Lichtervelde, M., Salvi, S., Béziat, D., and Linnen, R.L. (2007) Textural features and
753 chemical evolution in tantalum oxides: Magmatic versus hydrothermal origins for Ta
754 mineralization in the Tanco Lower Pegmatite, Manitoba, Canada. Economic Geology, 102,
755 257-276.
756 Van Lichtervelde, M., Holtz, F., and Hanchar, J.M. (2010) Solubility of manganotantalite, zircon
757 and hafnon in highly fluxed peralkaline to peraluminous pegmatitic melts. Contributions to
758 Mineralogy and Petrology, 160, 17-32.
759 Wang, R.S., Fontan, F., Xu, S.J., and Chen, X.M. (1997) The association of columbite, tantalite
760 and tapiolite in the Suzhou granite, China. Canadian Mineralogist, 35, 699- 706.

761 Wise, M.A., Turnock, A.C., and Černý, P. (1985) Improved unit cell dimensions for ordered
762 columbite-tantalite end-members. Neues Jahrbuch für Mineralogie – Monatshefte, 1985,
763 372-378.
764 Wise, M.A., and Černý, P. (1996) The crystal chemistry of the tapiolite series. Canadian
765 Mineralogist, 34, 631-647.
766 Wise, M.A., Francis, C.A., and Černý P. (2012) Compositional and structural variations in
767 columbite-group minerals from granitic pegmatites of the Brunswick and Oxford fields,
768 Maine: differential trends in F-poor and F-rich environments. Canadian Mineralogist, 50,
769 1515-1530.
770 Yang, Z., Song, R., Tao, K., and Zhang, P. (2003) Columbite – tantalite minerals from Nanping
771 granitic pegmatites, South China: compositional trends and genetic implications. Neues
772 Jahrbuch für Mineralogie – Monatshefte, 8, 363-373.
773 Zaraiski, G.P., Korzhinskaya, V., and Kotova, N. (2010) Experimental studies of Ta_2O_5 and
774 columbite–tantalite solubility in fluoride solutions from 300 to 550°C and 50 to 100 MPa:
775 Mineralogy and Petrology, 99, 287-300.
776 Zema, M., Tarantino, S.C., and Giorgiani, A. (2006) Structural changes induced by cation
777 ordering in ferrotapiolite. Mineralogical Magazine, 70, 319-328.

778 **Figure captions**

779 Figure 1. Mn* atomic ratios in glass and crystals for all experiments saturated in tantalite only
780 (grey triangle down), tapiolite only (grey triangle up) and both minerals (black symbols linked
781 with dash lines). The linear 1:1 crystal-melt correlation for each mineral phase suggests that the
782 activity coefficients are constant for all members of the Fe-Mn solid solution, so concentrations

783 can be used instead of activities in calculation solubility products.

784 Figure 2. Solubility products for $(Fe,Mn)(Nb,Ta)_2O_6$, irrespective of tapiolite or CGM, for
785 experiments saturated in tantalite only (diamonds), tapiolite only (squares) and both minerals
786 (triangles), at different conditions of temperature and pressure. The 3 upper ranges are for 200
787 MPa, and the lower range is for 50 MPa. Circled symbols are Nb-bearing experiments. Large
788 circles are solubility data at Mn*=1 from dissolution experiments from Van Lichtervelde et al.
789 (2010). Standard deviation (SD) on Mn* is calculated as 2σ. Error bars are not shown when they
790 are smaller than the symbol.

791 Figure 3. FEG-SEM images of crystal products in run Nb12 (50 MPa, 800ºC) showing
792 heterogeneous Ta* values in both tapiolite (a) and tantalite (b). Those heterogeneities are
793 principally encountered in experiments at 50 MPa.

794 Figure 4. TEM results on a FIB milled TEM foil cut from experiment Nb12. (**a**) Secondary
795 electron image of the foil showing zoned crystals. (**b**) Qualitative analyses of low-Ta* and high-
796 Ta* zones in tantalite. (**c**) Line scan across a zoned tantalite crystal using Fe Kα, Mn Kα, Nb Lα
797 and Ta Mα X-ray intensities, showing that the low-Ta* cores are oscillatory-zoned with respect to
798 Nb-Ta.

799 Figure 5. SEM image and chemical composition of the reverse experiment DBR showing the
800 reaction between a natural manganotantalite and a Fe-Nb-doped glass that produces columbite
801 and tapiolite. The gap limits are those determined at 200 MPa and 800ºC (see Figure 7).

802 Figure 6. Ternary diagram for Ti-bearing experiments showing the solid solution between

CGM/tapiolite and rutile. White symbols are tapiolite and grey ones are tantalite.

Figure 7. Composition of experimental products in the CGM quadrilateral, for different temperatures at 200 MPa (**left**), and for various conditions at 800ºC (**right**). Different symbols represent different experiments. In black are the experiments where tapiolite and tantalite coexist, in grey the experiments with only one mineral phase. At 200 MPa, the dotted vertical lines delimit the compositional gap at Ta*=1 for comparison between the different temperatures. The compositional gap at 200 MPa and 800ºC is drawn as dash lines for comparison in other plots.

Figure 8. CGM and tapiolite analyses from natural samples of the coltan fingerprinting database where the two minerals coexist. The tielines join analyses of mineral pairs coexisting as cogenetic phases in the same crystal (e.g., Figure 9). The compositional fields of cogenetic CGM and tapiolite are outlined in hatched areas and correspond to the gap limits. Samples are from Democratic Congo (CD), Rwanda (RW) and Nigeria (NG).

Figure 9. Details of CGM and tapiolite compositional evolution in two pegmatites from Rwanda (samples 089 on the left and 137 on the right), showing core to rim variations in both mineral phases (arrows). The hatched areas correspond to the gap limits as defined in Figure 8.

Figure 10. Literature compilation of coexisting CGM-tapiolite data worldwide. (**a**) Data from Abella et al. (1995), Anderson et al. (1998), Chudik et al. (2008), Küster et al. (2009), Llorens and Moro (2010), Neiva et al. (2008) and Van Lichtervelde et al. (2007). (**b**) Data from Novàk et al. (2000; 2003), Selway et al. (2005), Tindle and Breaks (2000), Wang et al. (1997) and Yang et al. (2003). (**c**) Data from the compilation of Černý et al. (1992) with their gap limits.

Figure 11. A vs. B site occupancy, in apfu, for crystalline products at 800ºC, showing that CGM and tapiolite crystallized at 200 MPa have a better stoichiometry than those at 50 MPa.

Figure 12. Comparison between the natural gap limits (hatched areas) separating the tapiolite and CGM fields and the gap limits determined from our experimental products at 800ºC (black curves; all experiments with coexisting tantalite and tapiolite). The dotted line is the gap at 50 MPa. The dashed lines represent the limits of the high Ta* compositions in tapiolite and low Ta* compositions in tantalite, and can be considered as the compositional limits for disequilibrium phases that formed at high degrees of supersaturation.

Appendix

Theoretical Gibbs Free Energy changes ($\Delta_f G°$) for the crystallization reactions of CGM end-members, calculated from the $\Delta_f G°$ of pure oxide constituents (for example, $\Delta_f G°$ of $FeTa_2O_6$ is the sum of the $\Delta_f G°$ of FeO and Ta_2O_5). Thermodynamic data from Hong and Kim (A thermodynamic study of the tantalum-oxygen system, 2001, U.S. Department of Energy Office of Scientific and Technical Information, Technical Report), Jacob et al. (Thermodynamic properties of niobium oxides, 2010, J. Chem. Eng. Data 55, 4854-4863) and Robie and Hemingway (USGS bulletin 2131, 1995).

Figure 1

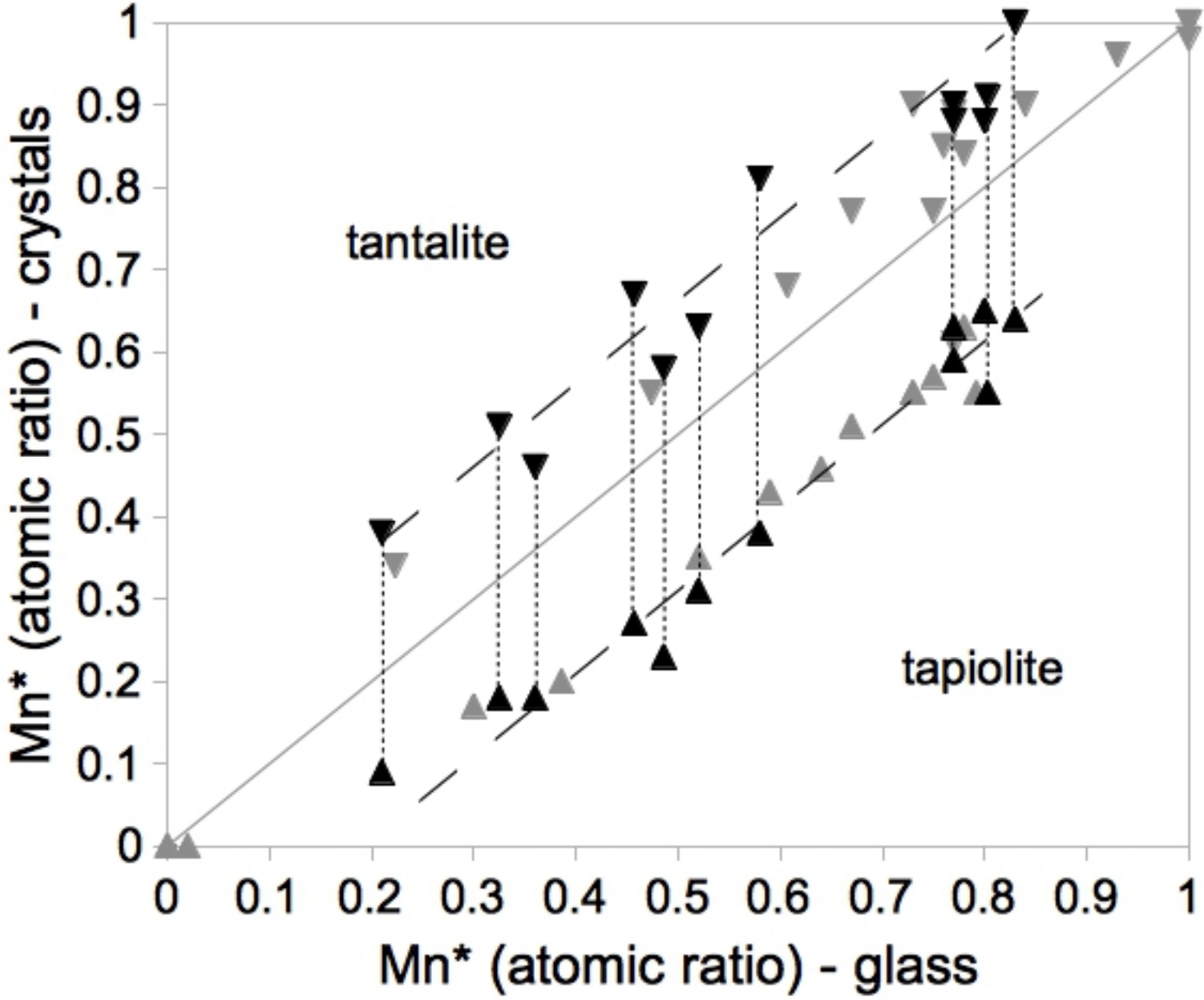
Mn* (atomic ratio) - crystals
Mn* (atomic ratio) - glass
tantalite
tapiolite
0
0.1
0.2
0.3
0.4
0.5
0.6
0.7
0.8
0.9
1

Figure 2

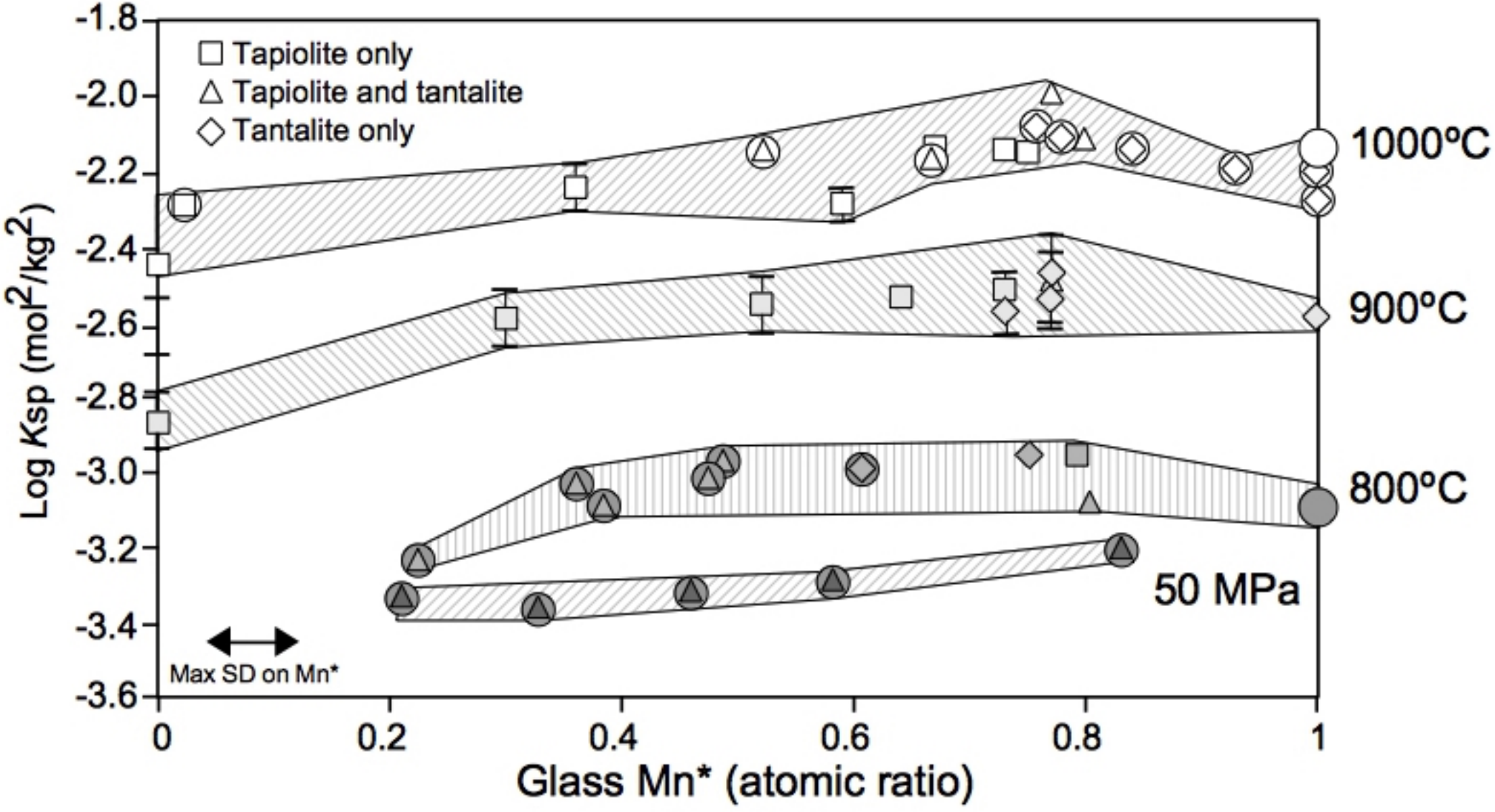
Tapiolite only
Tapiolite and tantalite
Tantalite only
1000°C
900°C
800°C
50 MPa
Max SD on Mn*
Log Ksp (mol²/kg²)
Glass Mn* (atomic ratio)
-1.8
-2.0
-2.2
-2.4
-2.6
-2.8
-3.0
-3.2
-3.4
-3.6
0
0.2
0.4
0.6
0.8
1

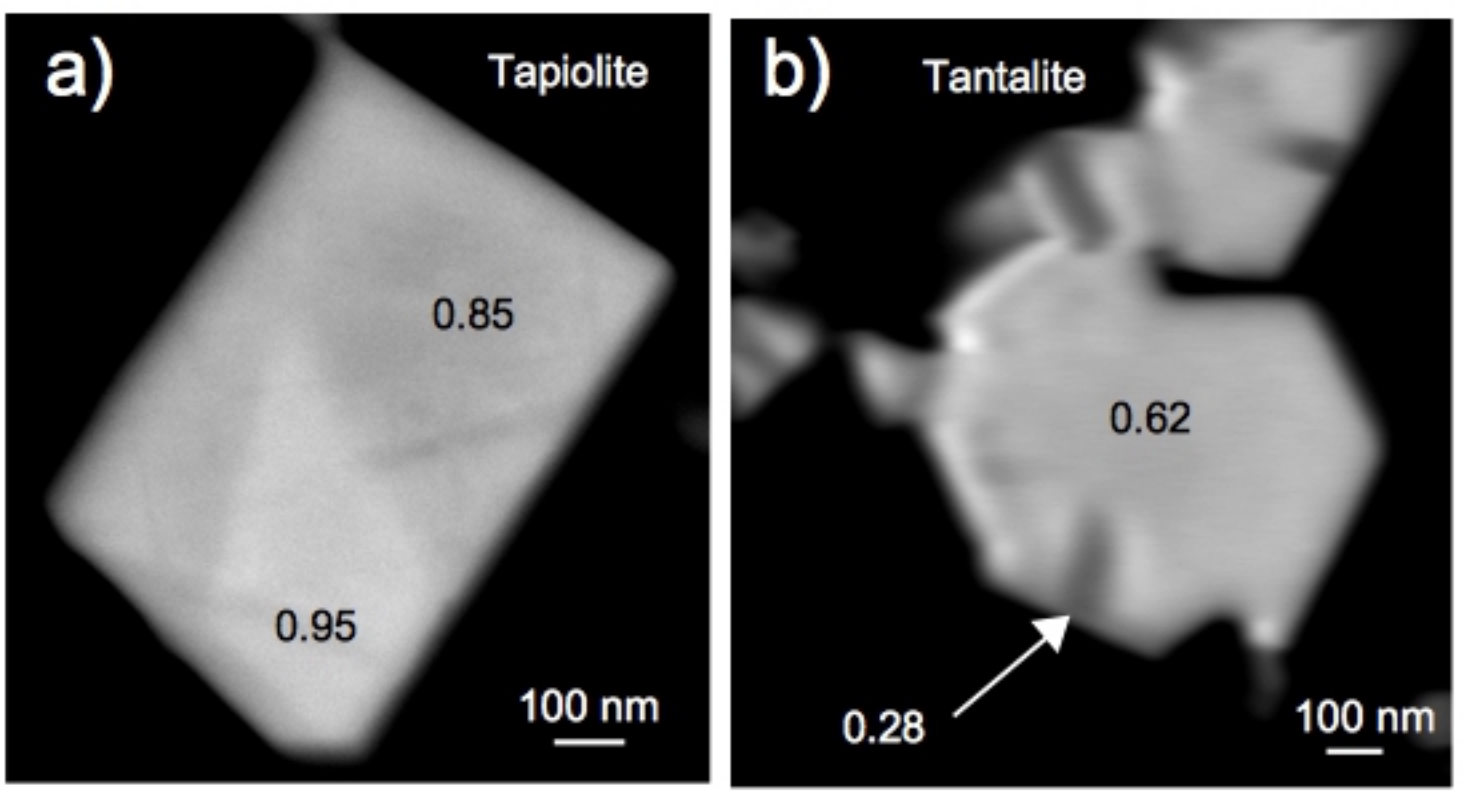
a)
Tapiolite
0.85
0.95
100 nm
b)
Tantalite
0.62
0.28
100 nm

Figure 4

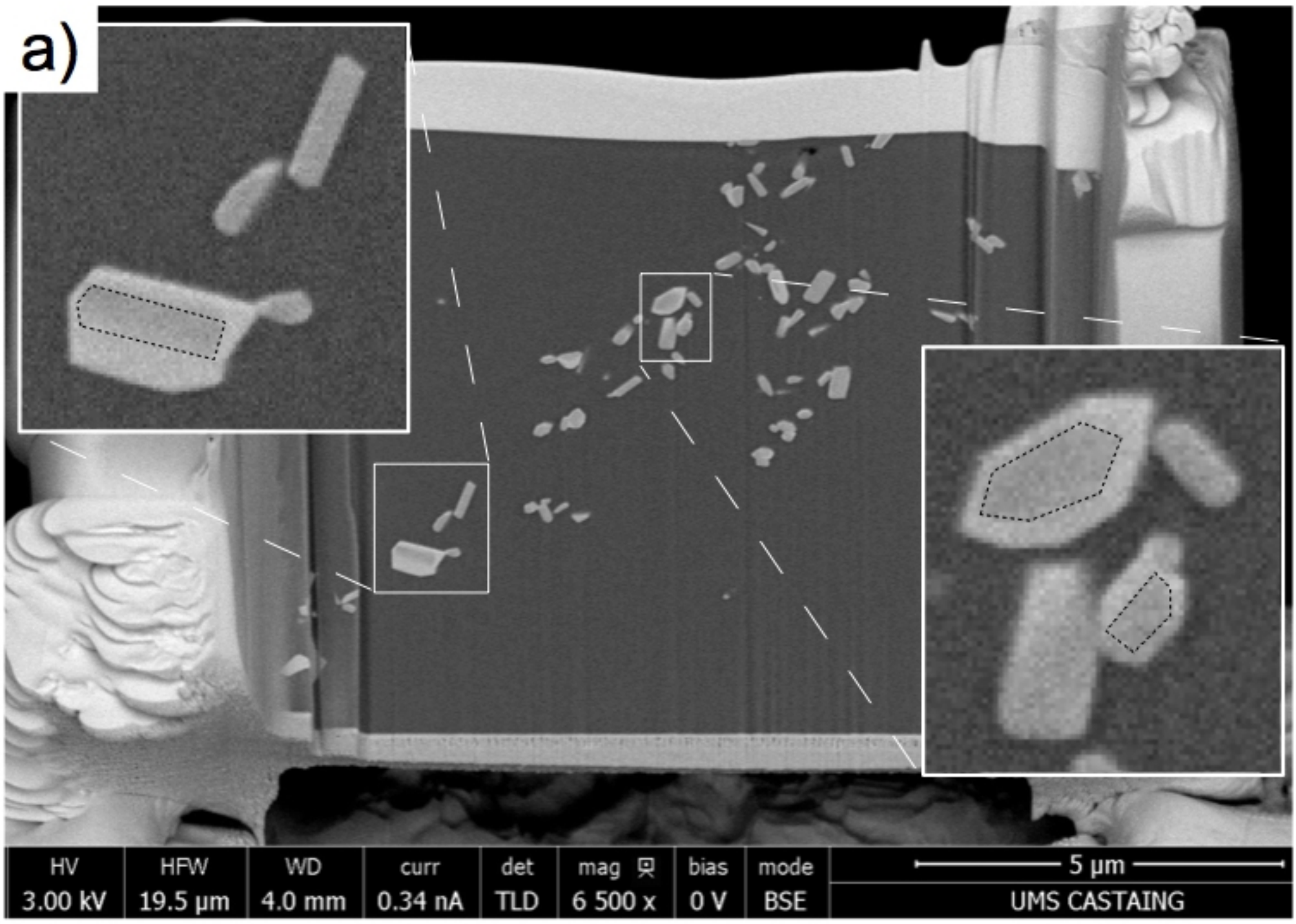
a)
HV
3.00 kV
HFW
19.5 µm
WD
4.0 mm
curr
0.34 nA
det
TLD
mag
6 500 x
bias
0 V
mode
BSE
5 µm
UMS CASTAING

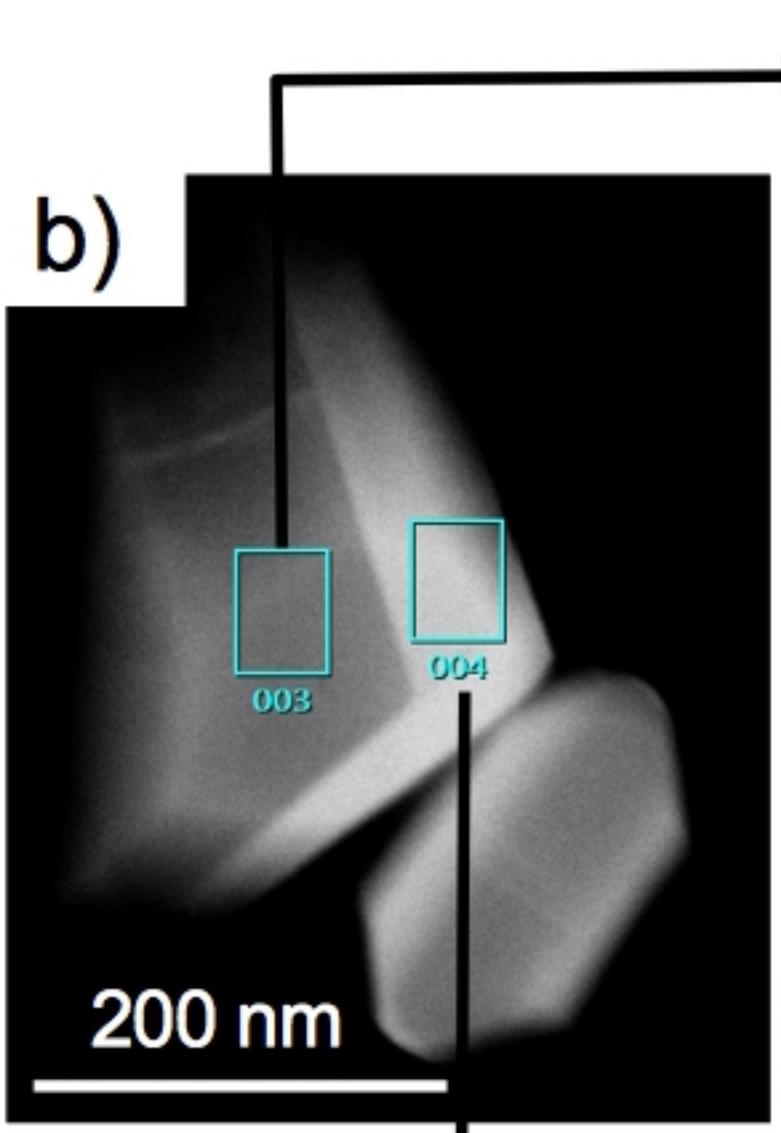
b)
003
004
200 nm

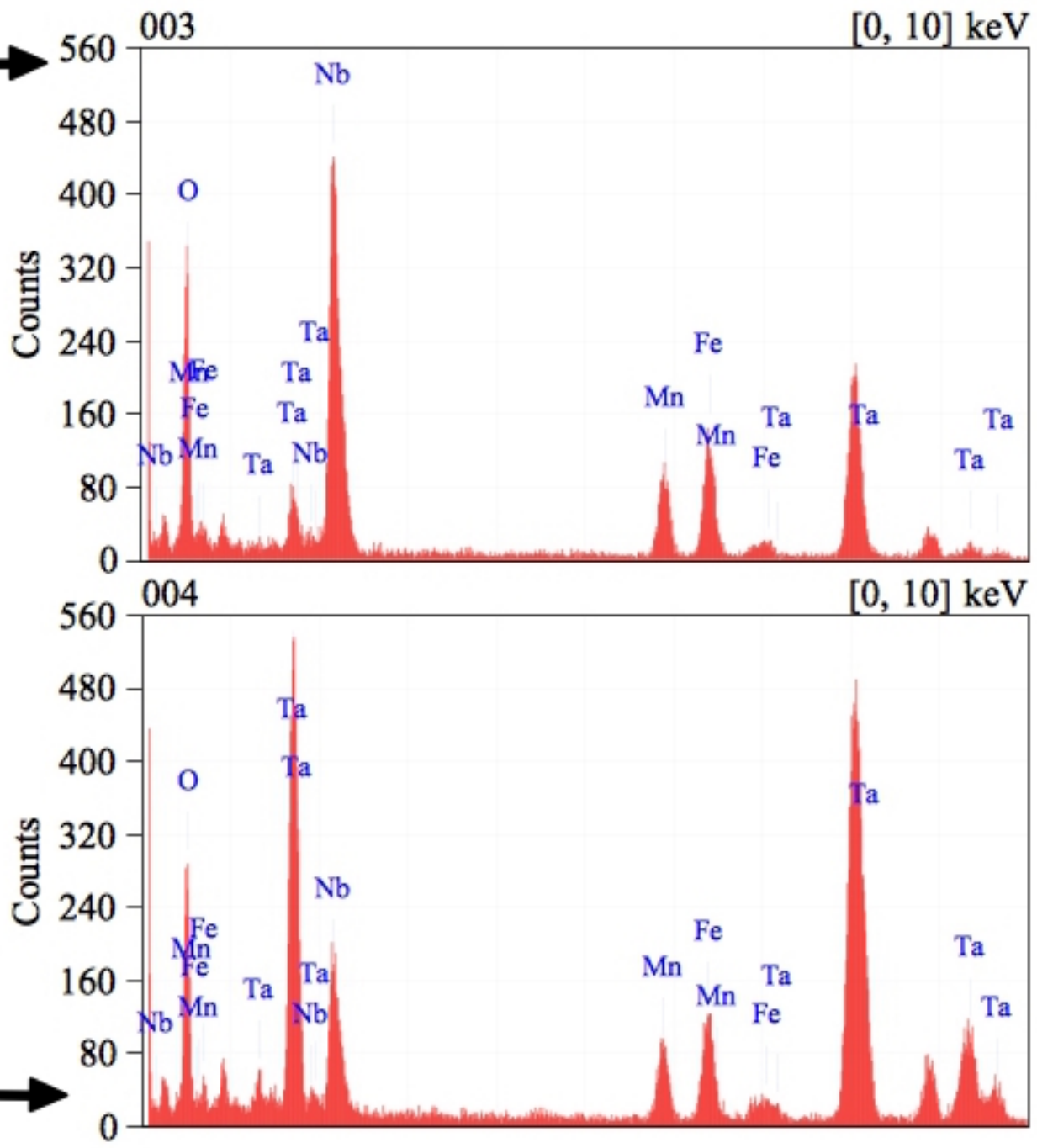
003
[0, 10] keV
Counts
Nb
O
Fe
Mn
Ta
004
[0, 10] keV
Counts

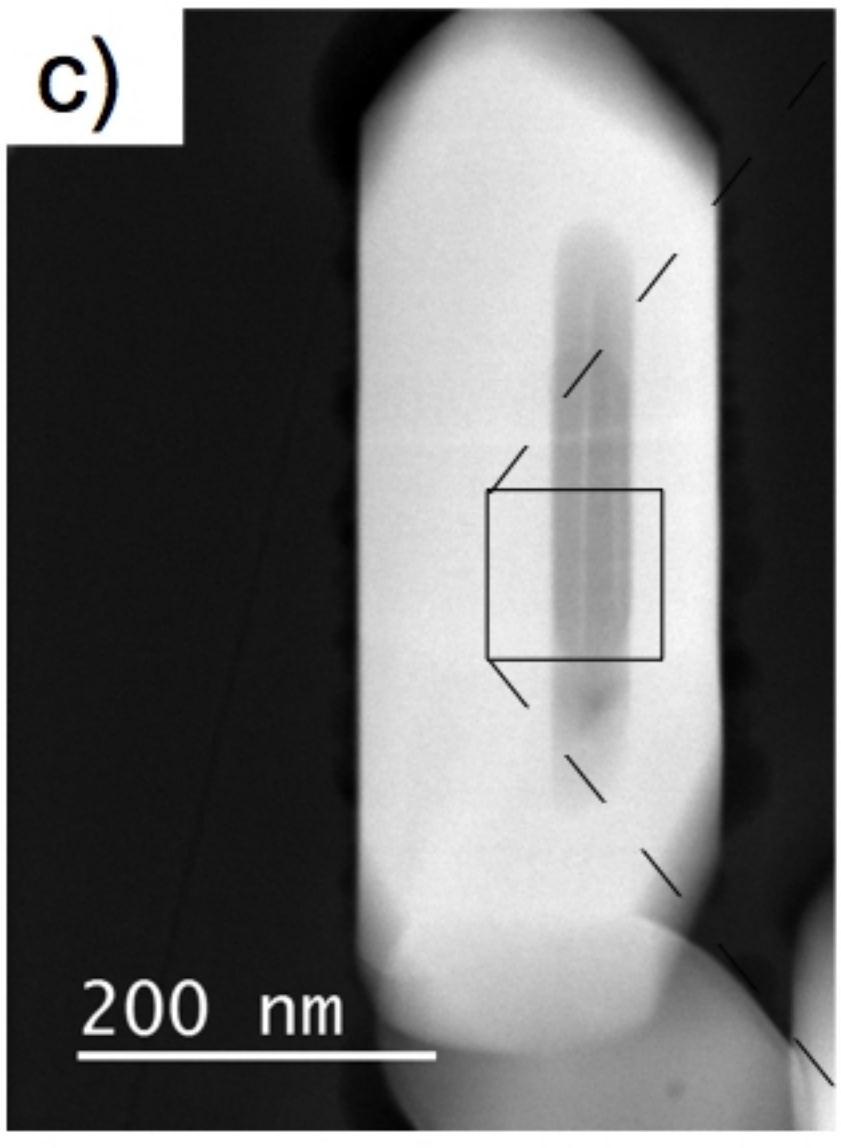
c)
200 nm

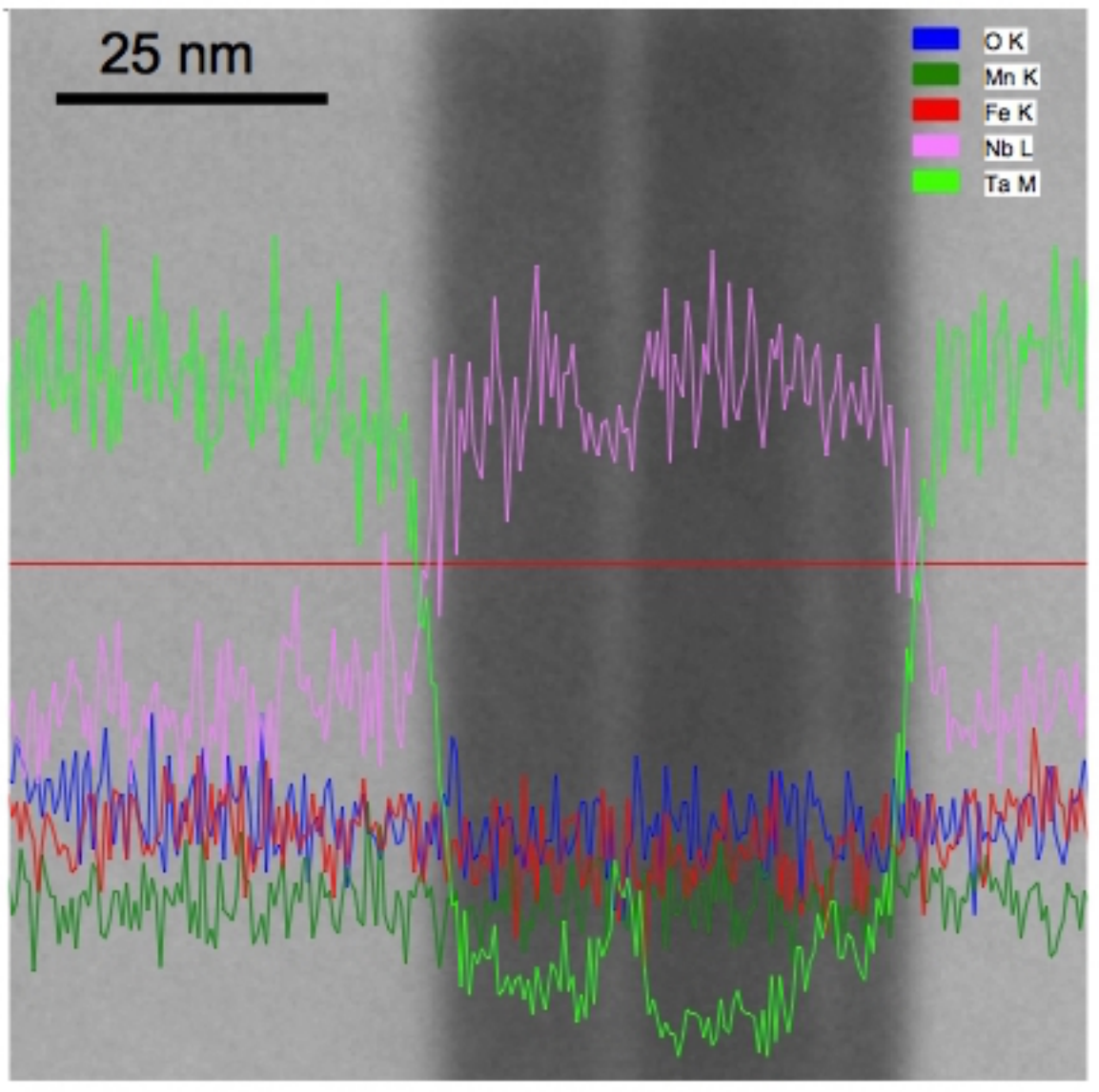
25 nm
O K
Mn K
Fe K
Nb L
Ta M

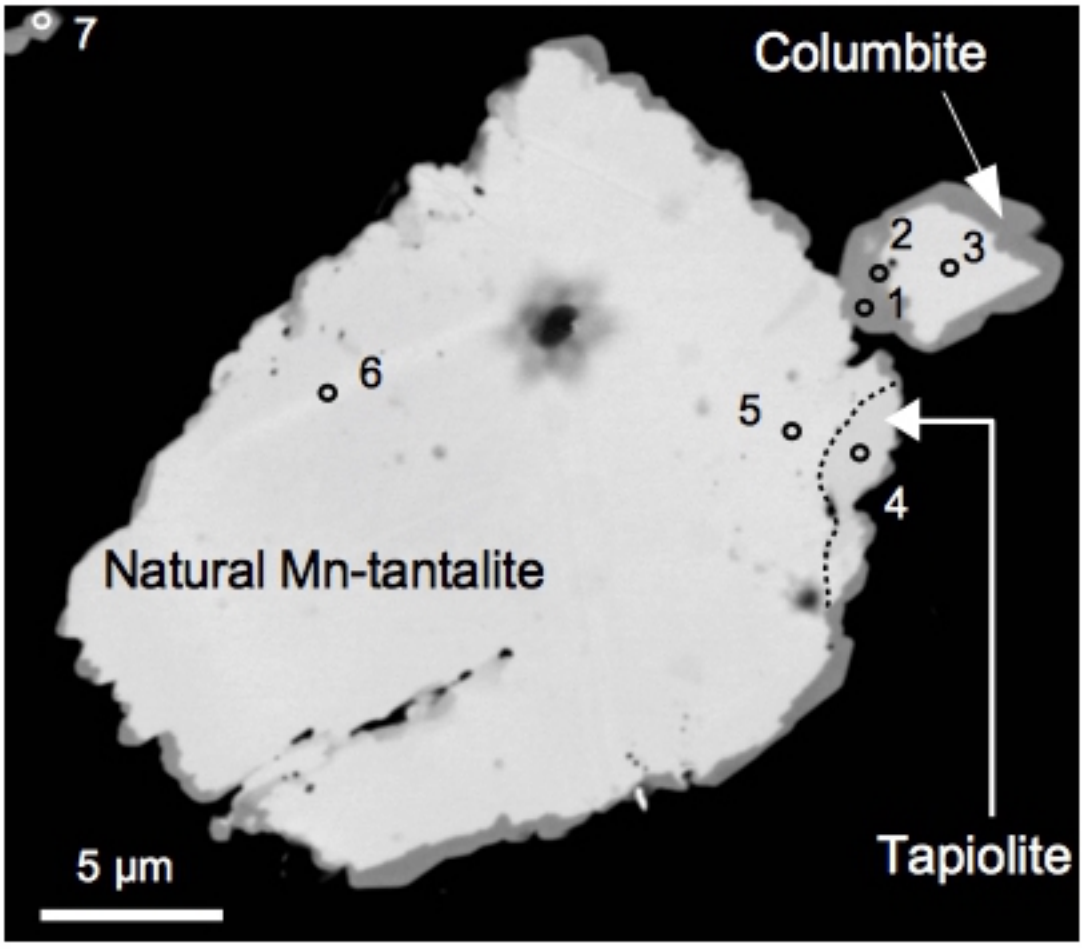
7
Columbite
2
3
1
6
5
4
Natural Mn-tantalite
5 µm
Tapiolite

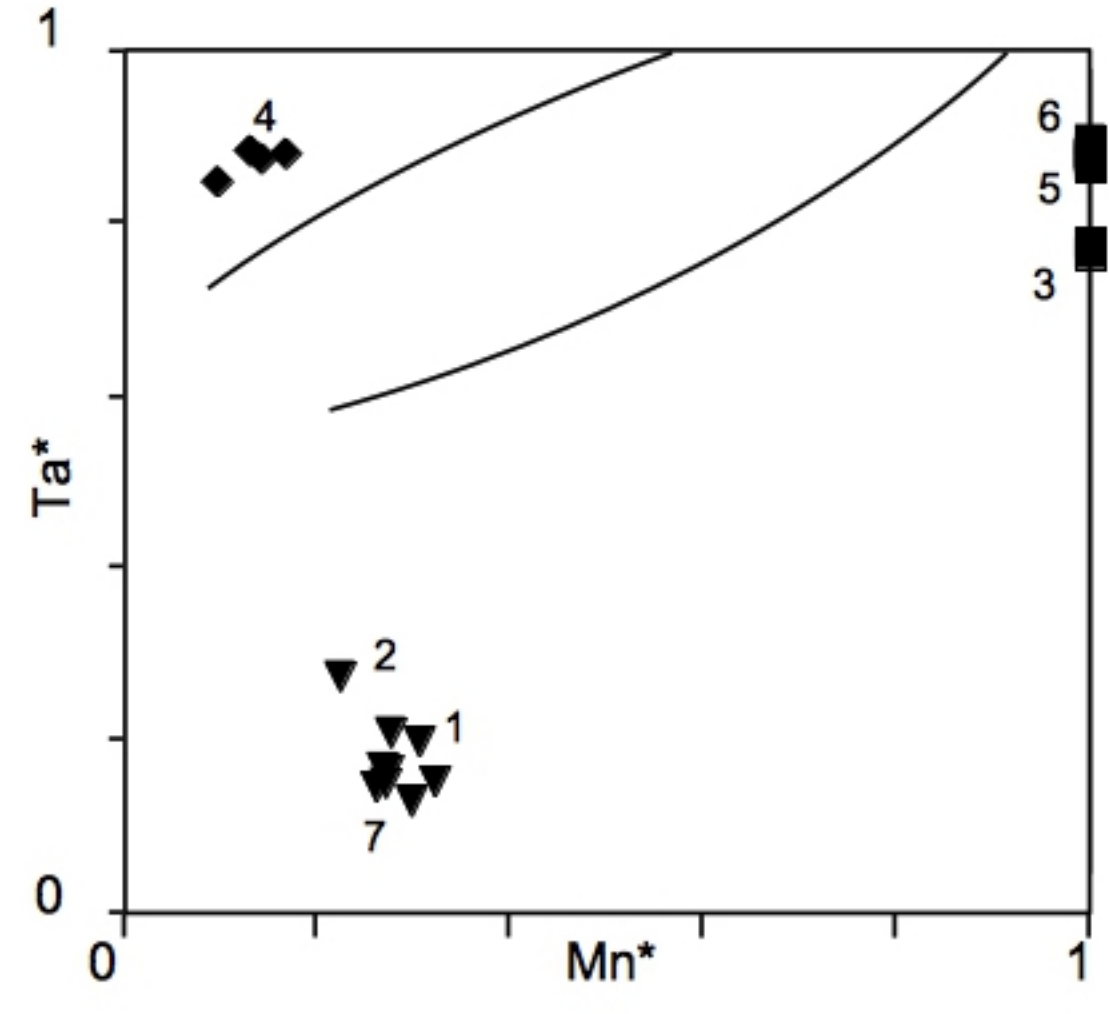
1
4
6
5
3
Ta*
2
1
7
0
0
Mn*
1

Figure 6

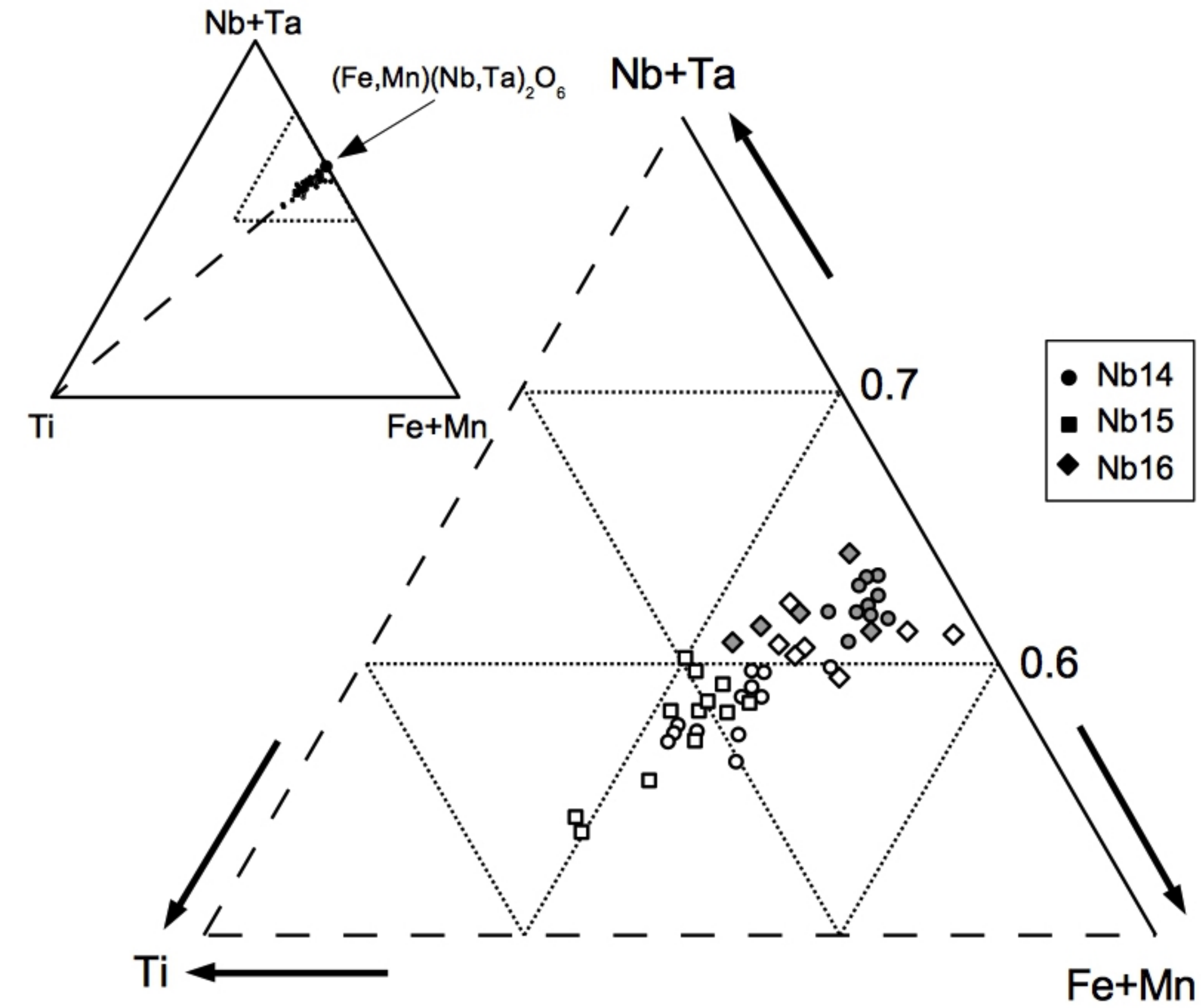

Figure 7

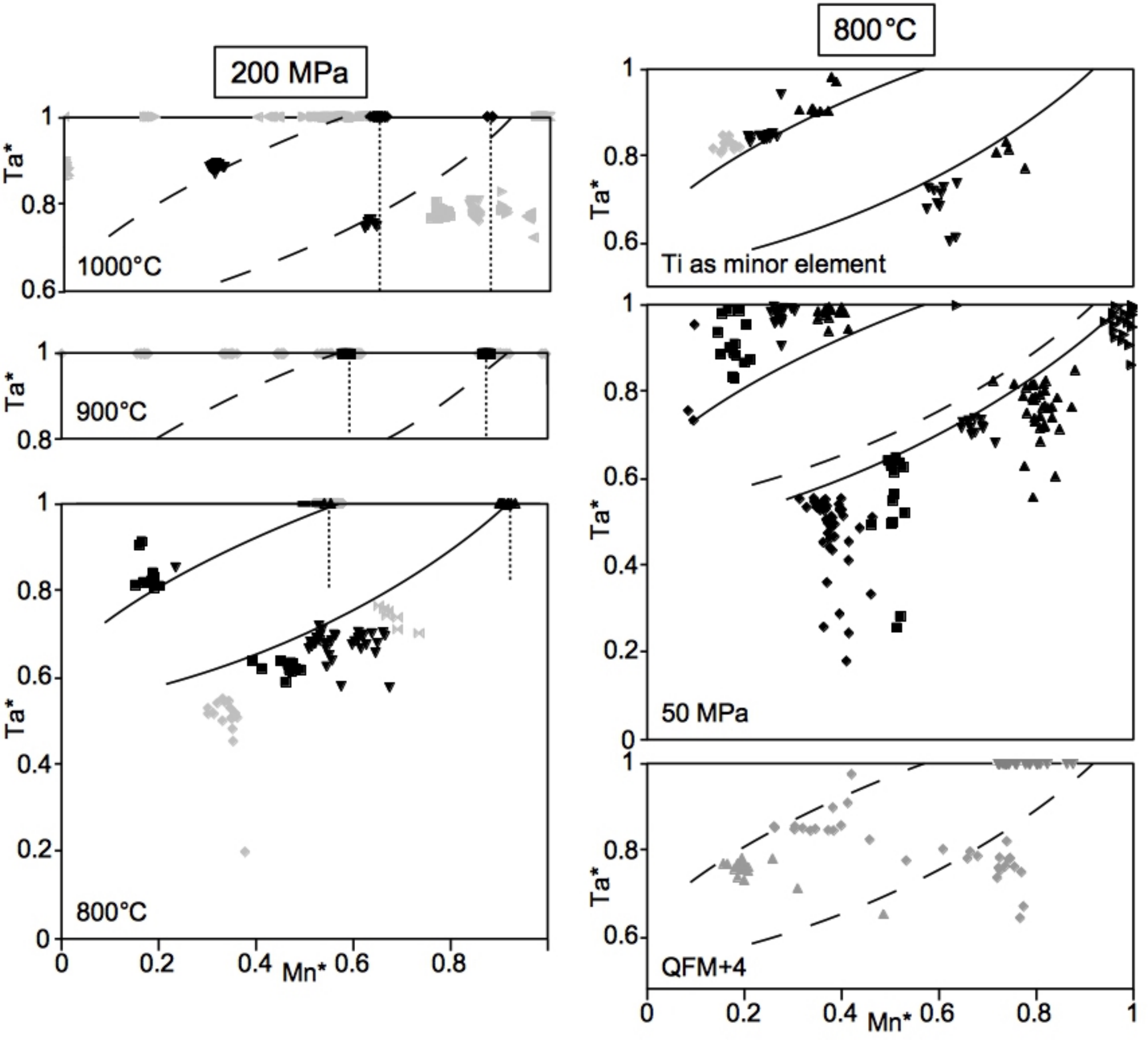
200 MPa
800°C
1000°C
900°C
800°C
Ti as minor element
50 MPa
QFM+4
Ta*
Mn*
0
0.2
0.4
0.6
0.8
1

Figure 8

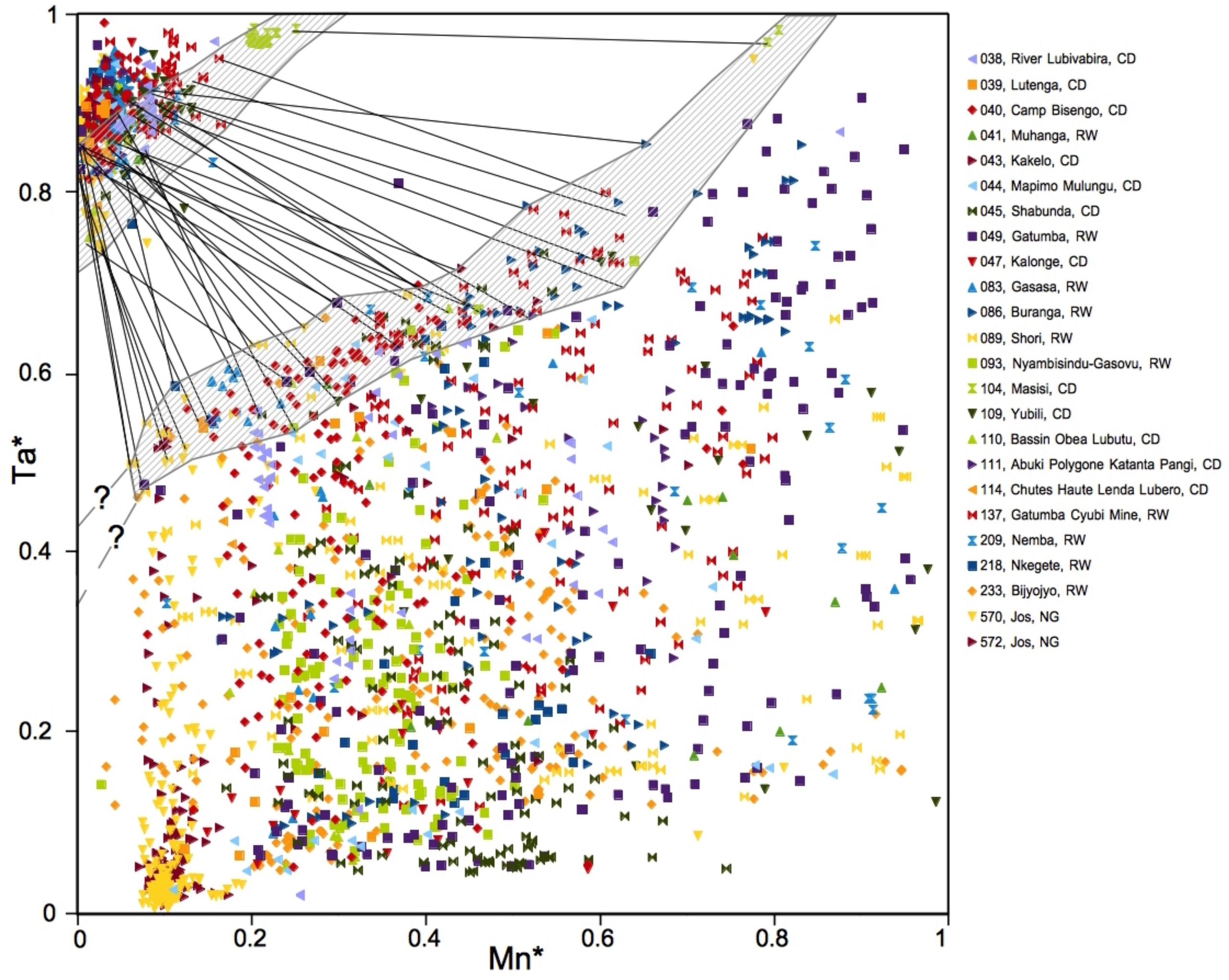
1
0.8
0.6
0.4
0.2
0
Ta*
?
?
0
0.2
0.4
0.6
0.8
1
Mn*
038, River Lubivabira, CD
039, Lutenga, CD
040, Camp Bisengo, CD
041, Muhanga, RW
043, Kakelo, CD
044, Mapimo Mulungu, CD
045, Shabunda, CD
049, Gatumba, RW
047, Kalonge, CD
083, Gasasa, RW
086, Buranga, RW
089, Shori, RW
093, Nyambisindu-Gasovu, RW
104, Masisi, CD
109, Yubili, CD
110, Bassin Obea Lubutu, CD
111, Abuki Polygone Katanta Pangi, CD
114, Chutes Haute Lenda Lubero, CD
137, Gatumba Cyubi Mine, RW
209, Nemba, RW
218, Nkegete, RW
233, Bijyojyo, RW
570, Jos, NG
572, Jos, NG

Figure 9

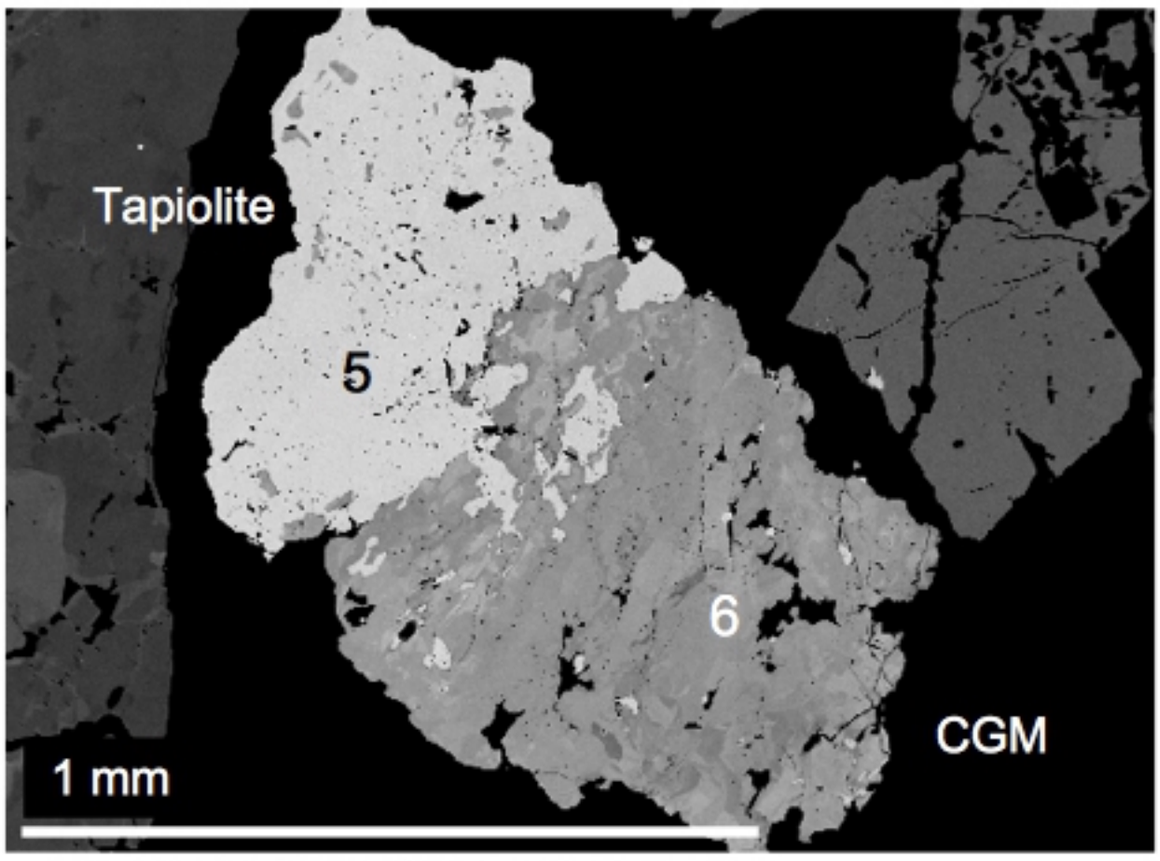
Tapiolite
5
6
CGM
1 mm

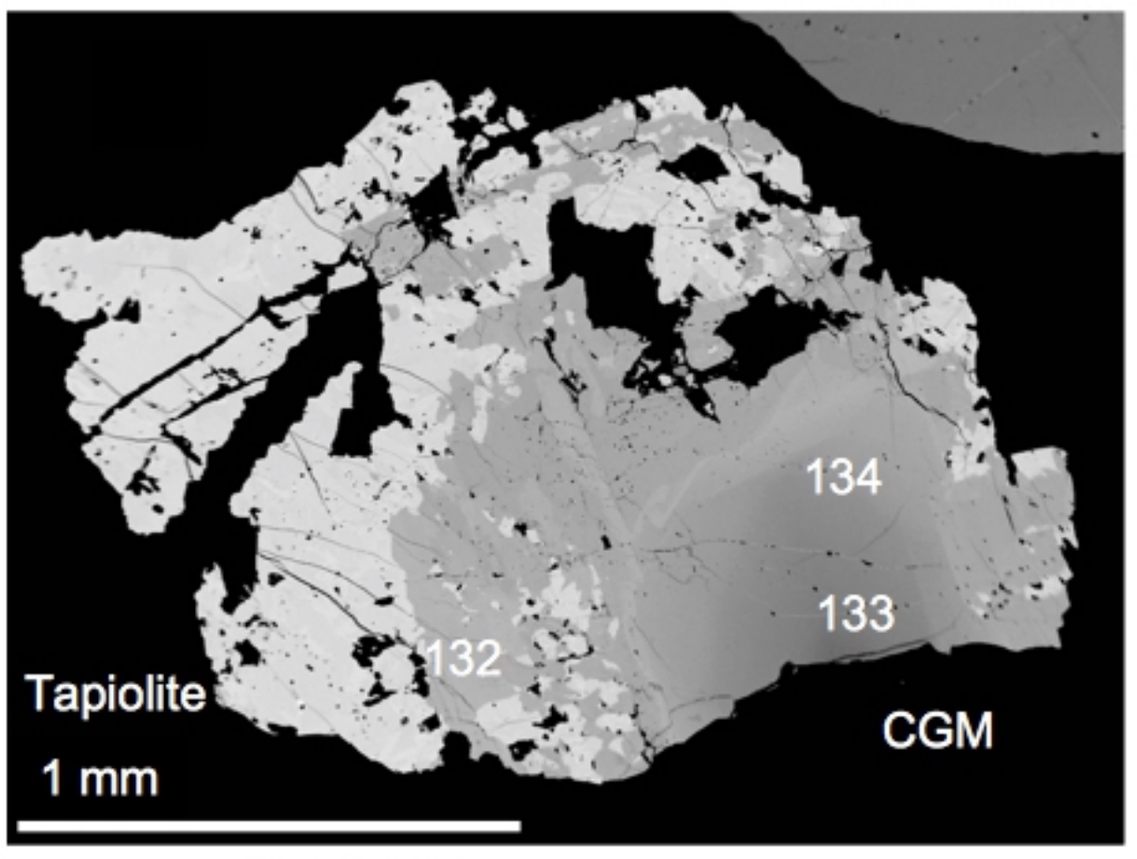
134
133
132
Tapiolite
CGM
1 mm

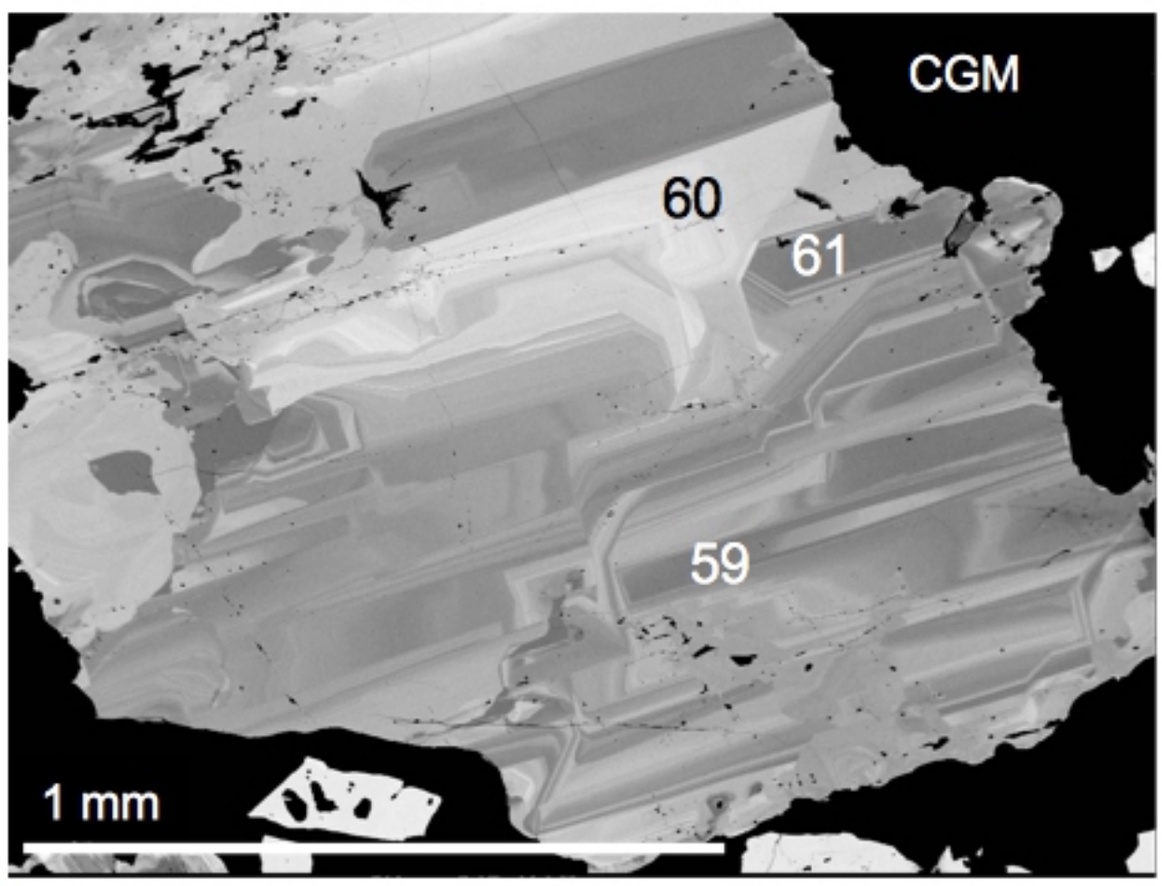
CGM
60
61
59
1 mm

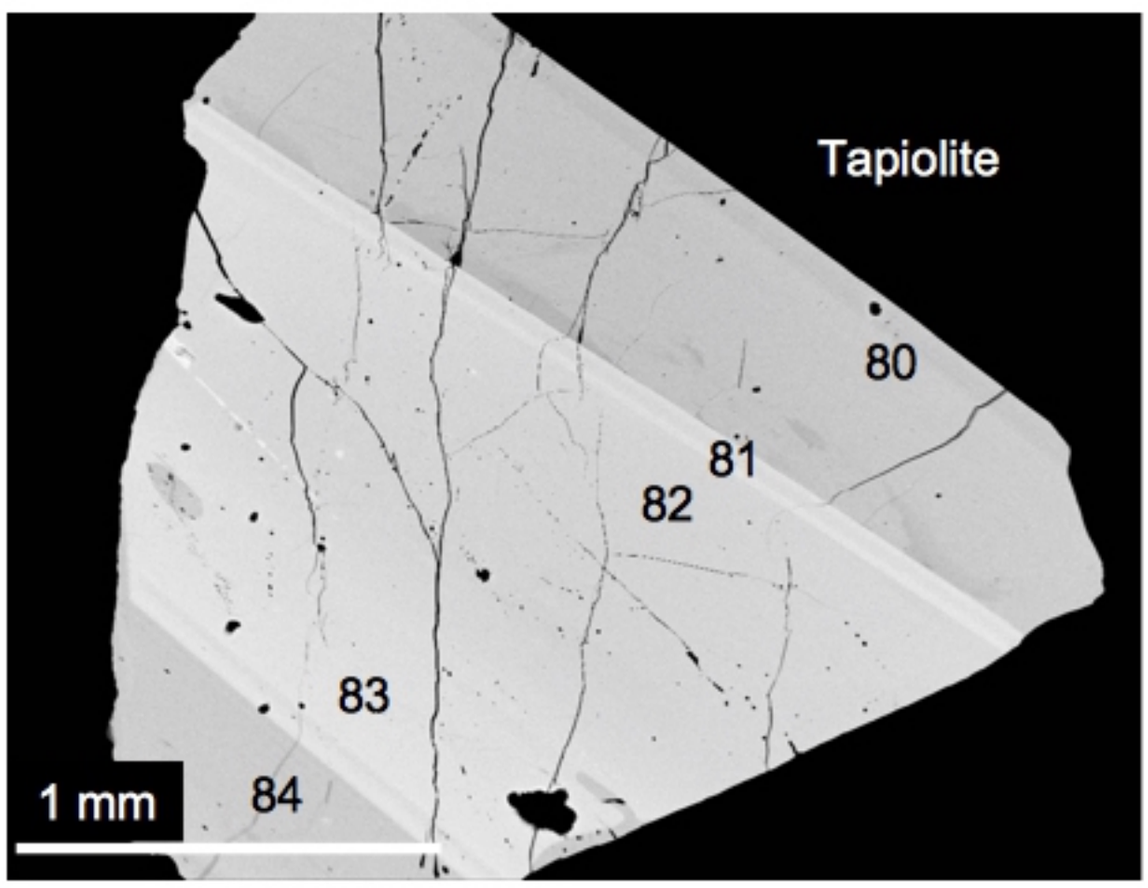
Tapiolite
80
81
82
83
84
1 mm

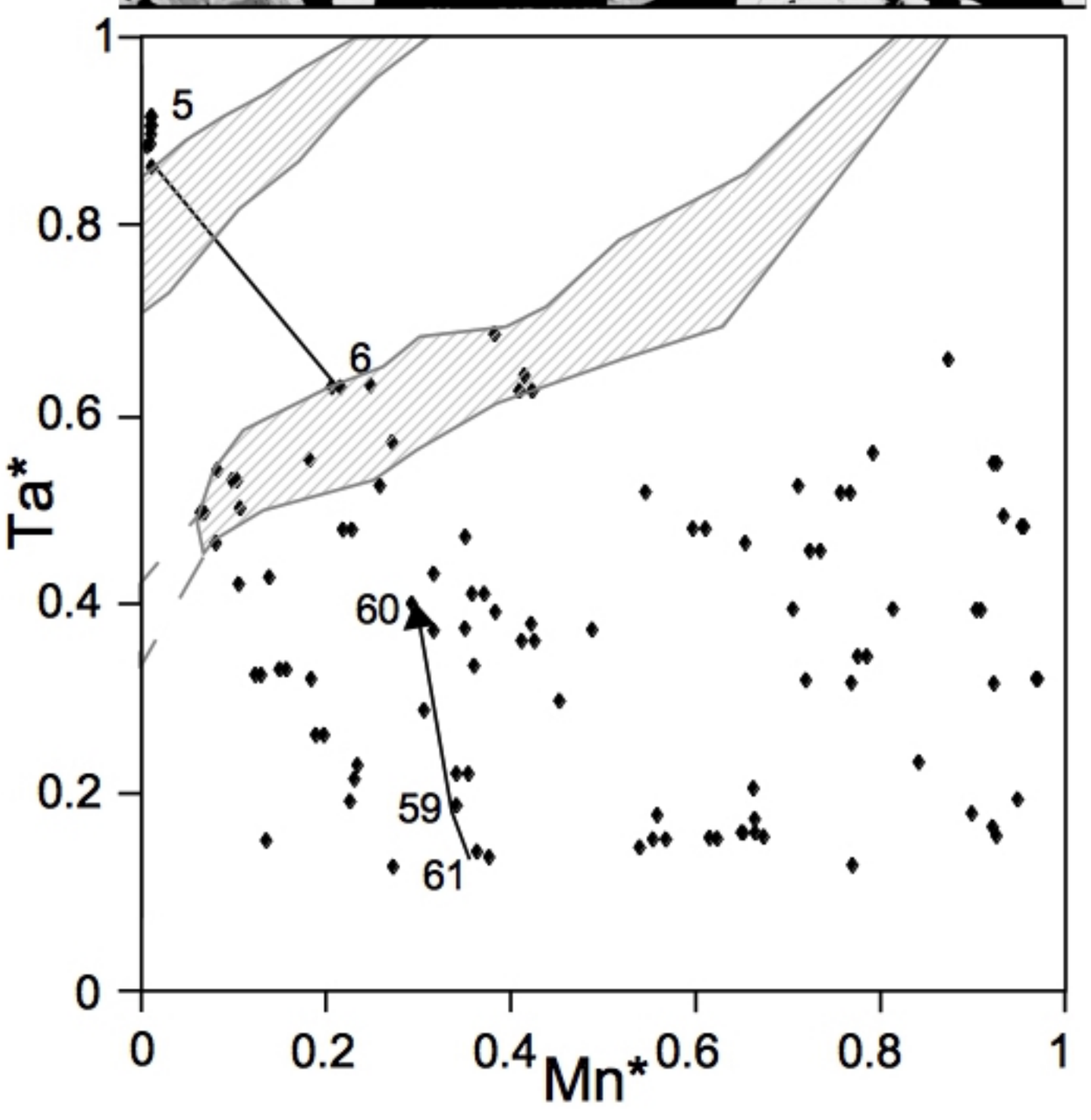
1
0.8
0.6
0.4
0.2
0
Ta*
0
0.2
0.4
0.6
0.8
1
Mn*
5
6
60
59
61

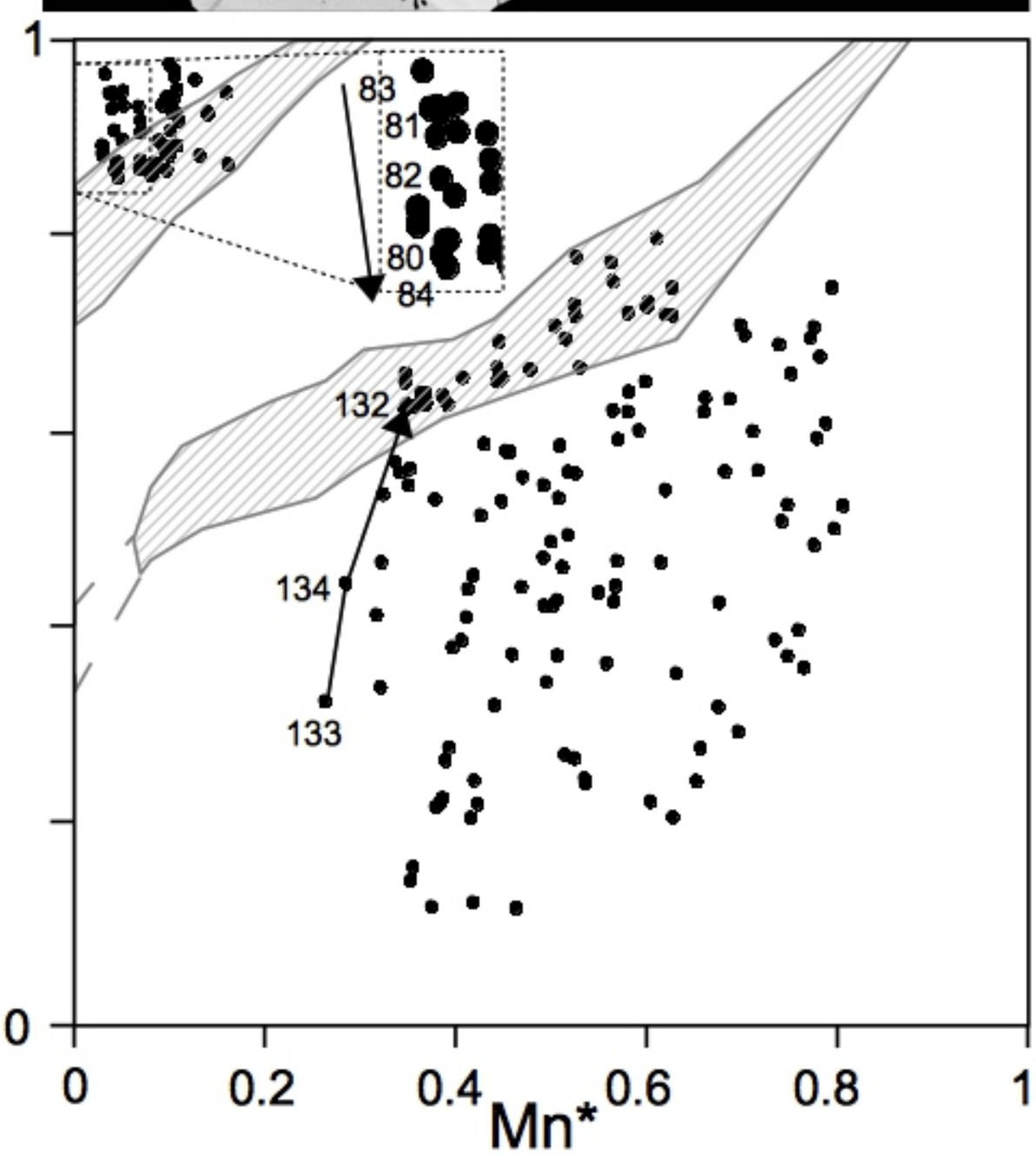
1
0
0.2
0.4
0.6
0.8
1
Mn*
83
81
82
80
84
132
134
133

Figure 10

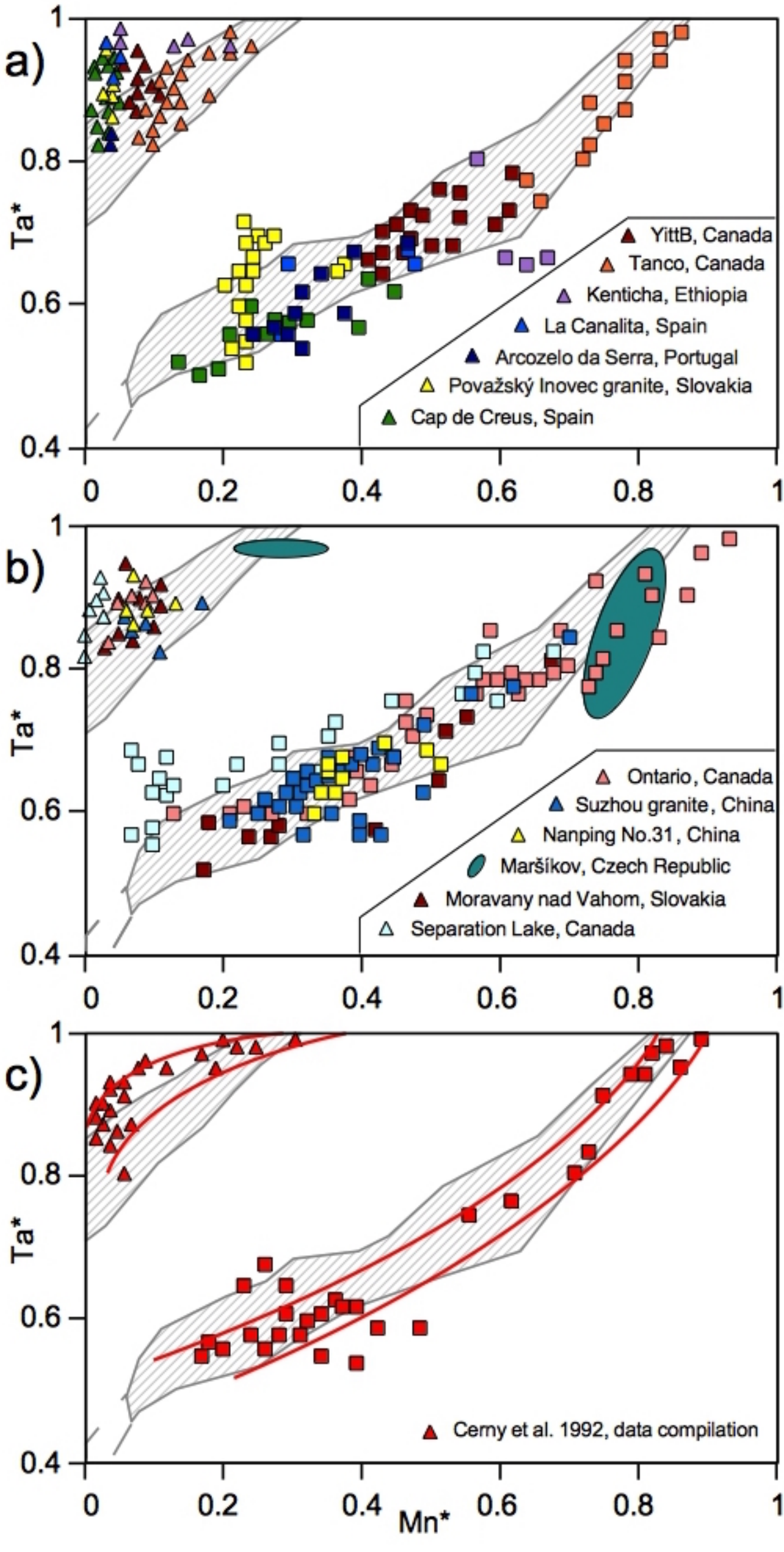
a)
b)
c)
Ta*
Mn*
0
0.2
0.4
0.6
0.8
1
YittB, Canada
Tanco, Canada
Kenticha, Ethiopia
La Canalita, Spain
Arcozelo da Serra, Portugal
Považský Inovec granite, Slovakia
Cap de Creus, Spain
Ontario, Canada
Suzhou granite, China
Nanping No.31, China
Maršíkov, Czech Republic
Moravany nad Vahom, Slovakia
Separation Lake, Canada
Cerny et al. 1992, data compilation

Figure 11

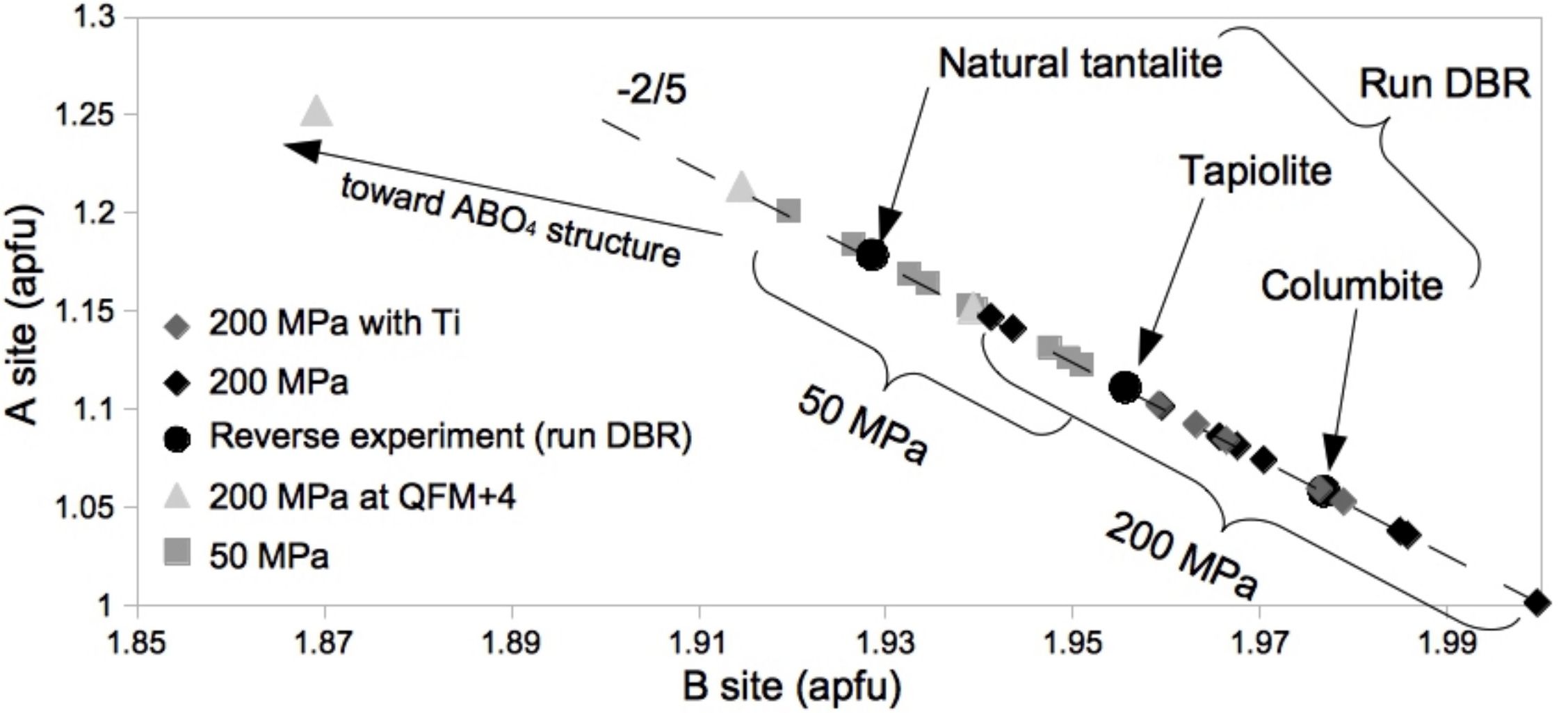
1.3
1.25
1.2
1.15
1.1
1.05
1
A site (apfu)
1.85
1.87
1.89
1.91
1.93
1.95
1.97
1.99
B site (apfu)
-2/5
toward ABO4 structure
Natural tantalite
Run DBR
Tapiolite
Columbite
50 MPa
200 MPa
200 MPa with Ti
200 MPa
Reverse experiment (run DBR)
200 MPa at QFM+4
50 MPa

Figure 12

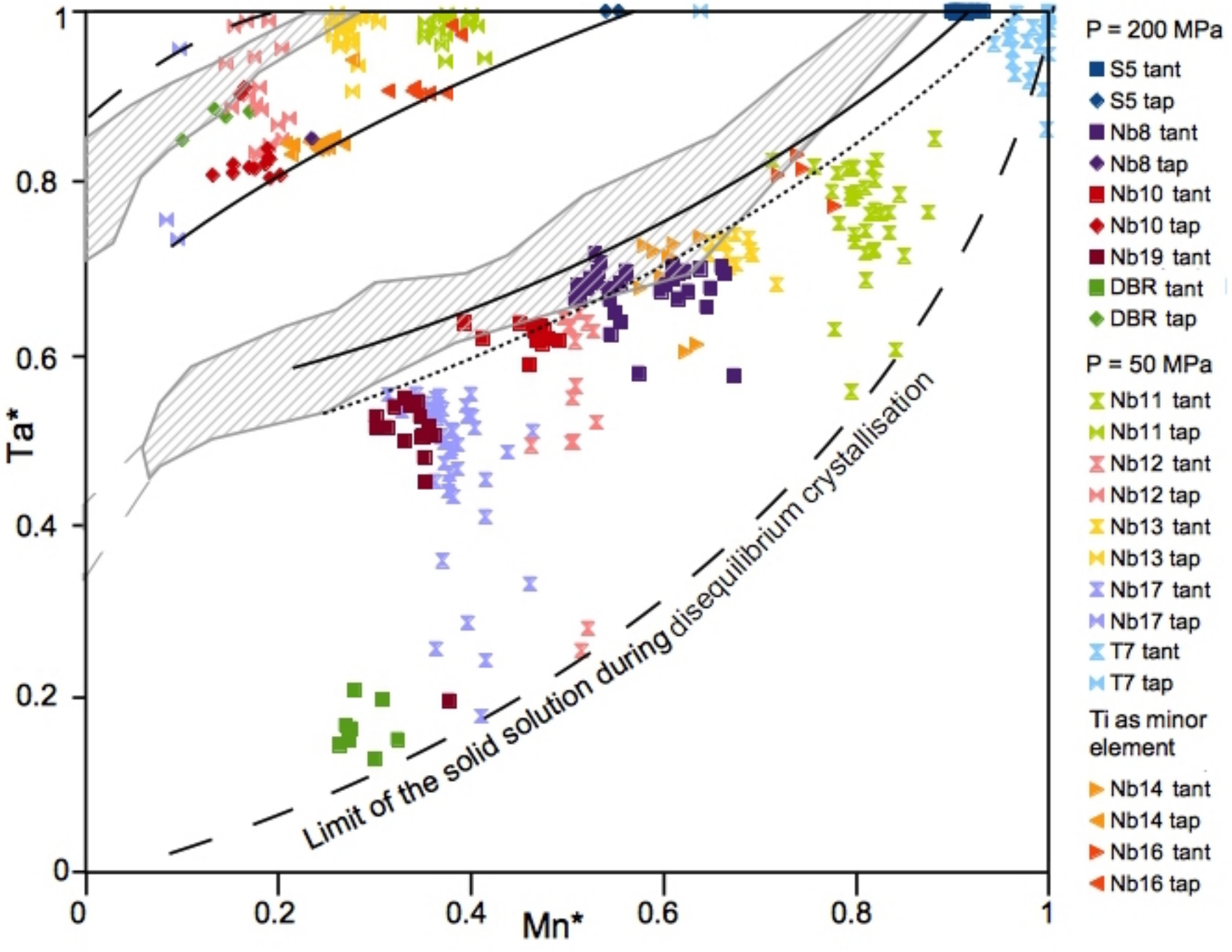
Ta*
Mn*
0
0.2
0.4
0.6
0.8
1
Limit of the solid solution during disequilibrium crystallisation
P = 200 MPa
S5 tant
S5 tap
Nb8 tant
Nb8 tap
Nb10 tant
Nb10 tap
Nb19 tant
DBR tant
DBR tap
P = 50 MPa
Nb11 tant
Nb11 tap
Nb12 tant
Nb12 tap
Nb13 tant
Nb13 tap
Nb17 tant
Nb17 tap
T7 tant
T7 tap
Ti as minor element
Nb14 tant
Nb14 tap
Nb16 tant
Nb16 tap

Table 1. Starting glass EPMA compositions (wt%)

	Undoped glass	Glass+MnTa	Glass+FeTa	Glass+MnNb	Glass+FeNb	Glass+Ti
n	10	45	24	13	10	20
SiO_2	66.92	60.83	58.04	63.25	62.25	65.98
Sd Dev	*1.52*	*0.43*	*2.14*	*2.16*	*2.47*	*3.18*
Al_2O_3	16.58	15.05	15.13	15.48	16.24	16.04
Sd Dev	*0.78*	*0.19*	*0.66*	*1.02*	*0.94*	*1.48*
Na_2O	3.07	2.58	2.67	2.95	3.04	2.99
Sd Dev	*0.13*	*0.15*	*0.21*	*0.19*	*0.34*	*0.24*
K_2O	5.71	5.32	5.51	5.61	5.59	5.70
Sd Dev	*0.2*	*0.07*	*0.16*	*0.10*	*0.13*	*0.21*
F	2.96	2.79	2.97	n.a.	n.a.	2.97
Sd Dev	*0.6*	*0.84*	*0.61*	*n.a.*	*n.a.*	*0.41*
P_2O_5	3.59	3.34	3.68	3.75	4.05	3.79
Sd Dev	*0.43*	*0.19*	*0.36*	*0.56*	*0.57*	*0.88*
MnO	0	1.4	0	1.31	0	0
Sd Dev		*0.18*		*0.18*		
FeO	0	0	1.45	0	1.55	0
Sd Dev			*0.2*		*0.18*	
Ta_2O_5	0	9.1	10.2	0	0	0
Sd Dev		*0.3*	*0.88*			
Nb_2O_5	0	0	0	5.09	5.05	0
Sd Dev				*0.53*	*0.68*	
TiO_2	0	0	0	0	0	1.72
Sd Dev						*0.22*
Total	98.83	100.41	99.65	97.44	97.76	99.19

In italic are standard deviations (*Sd Dev*) on *n* analyses

All glasses contain ~0.9 wt% Li_2O (non measured)

Table 2. Starting conditions of experimental runs

	Weight proportions of starting glasses						theoretical glass composition (wt%)						
run	1	Fe+Ta	Mn+Ta	Fe+Nb	Mn+Nb	Ti	MnO	Ta_2O_5	Nb_2O_5	FeO	TiO_2	Mn*	Ta*
A5	0	1	0				0.00	10.20		1.45		0.00	
A3	0.5	0.35	0.15				0.21	4.97		0.51		0.30	
A1	0	0.5	0.5				0.70	9.76		0.73		0.49	
A4	0.5	0.15	0.35				0.49	4.79		0.22		0.70	
A2	0.5	0	0.5				0.70	4.66		0.00		1.00	
A6	0	0	1				1.40	9.32		0.00		1.00	
A7	0.51	0.13	0.36				0.51	4.74		0.19		0.73	
A8	0.51	0.12	0.38				0.53	4.72		0.17		0.75	
A9	0.50	0.11	0.39				0.54	4.72		0.16		0.77	
A10	0.51	0.09	0.40				0.56	4.67		0.14		0.81	
Nb1	0.5	0.4	0	0.1	0		0.00	4.08	0.51	0.74		0.00	0.85
Nb2	0.5	0	0.4	0	0.1		0.69	3.73	0.51	0.00		1.00	0.84
Nb6	0.49	0.03	0.38	0.02	0.08		0.63	3.82	0.52	0.07		0.90	0.84
Nb5	0.50	0.05	0.35	0.04	0.06		0.57	3.78	0.52	0.14		0.80	0.84
Nb7	0.5	0.06	0.34	0.05	0.05		0.54	3.78	0.51	0.17		0.76	0.84
Nb4	0.5	0.1	0.3	0.04	0.06		0.50	3.82	0.51	0.21		0.71	0.84
Nb3	0.5	0.2	0.2	0.05	0.05		0.34	3.90	0.51	0.37		0.48	0.85
B2	0	0.2	0.8				1.12	9.50		0.29		0.80	
B8	0	0.24	0.76				1.06	9.53		0.35		0.76	
B7	0	0.29	0.71				0.99	9.58		0.42		0.71	
B9	0	0.34	0.66				0.92	9.62		0.49		0.65	
B5	0	0.4	0.6				0.84	9.67		0.58		0.59	
B1	0	0.5	0.5				0.70	9.76		0.73		0.49	
B4	0	0.6	0.4				0.56	9.85		0.87		0.39	
B3	0	0.8	0.2				0.28	10.02		1.16		0.20	
B6	0	1	0				0.00	10.20		1.45		0.00	
B10	0	0	1				1.40	9.32		0.00		1.00	
S5	0.75	0.03	0.22				0.31	2.35		0.04		0.89	
T7 – 50MPa	0.73	0.03	0.24				0.34	2.53		0.04		0.89	
S6	0.75	0.04	0.21				0.30	2.39		0.06		0.84	
S3b – QFM+4	0.75	0.05	0.20				0.28	2.40		0.07		0.79	
Nb9	0.69	0.06	0.18	0.03	0.04		0.30	2.29	0.37	0.14		0.69	0.82
Nb11 – 50MPa	0.69	0.06	0.18	0.03	0.04		0.30	2.29	0.37	0.14		0.69	0.82
Nb16 – Ti	0.51	0.08	0.23	0.04	0.05	0.09	0.39	2.98	0.37	0.18	0.15	0.69	0.83
Nb8	0.69	0.12	0.12	0.04	0.04		0.21	2.32	0.38	0.24		0.48	0.82
Nb8b – QFM+4	0.50	0.19	0.20	0.06	0.06		0.35	3.80	0.56	0.37		0.49	0.83
Nb13 – 50MPa	0.69	0.12	0.12	0.04	0.04		0.21	2.32	0.38	0.24		0.48	0.82
Nb14 - Ti	0.54	0.14	0.14	0.04	0.05	0.09	0.25	2.69	0.46	0.27	0.15	0.49	0.81
Nb10	0.69	0.18	0.06	0.04	0.03		0.13	2.36	0.37	0.32		0.28	0.82
Nb10b – QFM+4	0.67	0.19	0.06	0.05	0.03		0.13	2.49	0.38	0.35		0.27	0.82
Nb12 – 50MPa	0.69	0.18	0.06	0.04	0.03		0.13	2.36	0.37	0.32		0.28	0.82
Nb15 – Ti	0.52	0.21	0.08	0.05	0.04	0.1	0.17	2.89	0.43	0.38	0.17	0.31	0.83
Nb17 – 50MPa	0.69	0.15	0.03	0.08	0.04		0.10	1.87	0.64	0.36		0.22	0.68
Nb19	0.69	0.15	0.03	0.08	0.04		0.10	1.87	0.64	0.36		0.22	0.68

Starting *T* [°C]	Final *T* [°C]	*P* [Mpa]	*f*O2
1050	1000	200	NNO+1.5
1050	1000	200	NNO+1.5
1050	1000	200	NNO+1.5
1050	1000	200	NNO+1.5
1050	1000	200	NNO+1.5
1050	1000	200	NNO+1.5
1050	1000	200	NNO+1.5
1050	1000	200	NNO+1.5
1050	1000	200	NNO+1.5
1050	1000	200	NNO+1.5
1050	1000	200	NNO+1.5
	1000	200	NNO-0.5
	1000	200	NNO-0.5
	1000	200	NNO-0.5
	1000	200	NNO-0.5
	1000	200	NNO-0.5
	1000	200	NNO-0.5
	1000	200	NNO-0.5
950	900	200	NNO+1.5
950	900	200	unknown
950	900	200	unknown
950	900	200	unknown
950	900	200	NNO+1.5
950	900	200	NNO+1.5
950	900	200	NNO+1.5
950	900	200	NNO+1.5
950	900	200	NNO+1.5
950	900	200	unknown
	800	200	NNO
	800	50	NNO
	800	200	NNO
	800	200	NNO+3
	800	200	NNO
500	800	50	NNO
	800	200	NNO
	800	200	NNO
	800	200	NNO+3
500	800	50	NNO
	800	200	NNO
	800	200	NNO
	800	200	NNO+3
500	800	50	NNO
	800	200	NNO
	800	50	NNO
	800	200	NNO

Table 3. EPMA analyses of experimental glasses

run	*n*	MnO	*SD*	FeO	*SD*	Ta_2O_5	*SD*	Nb_2O_5	*SD*	TiO_2	*SD*	Mn*	*SD*	Ta*	*SD*	logKsp	*SD*
A5	15	0	*0*	0.33	*0.05*	3.6	*0.65*					0	*0*			-2.44	*0.12*
A3	20	0.2	*0.07*	0.35	*0.07*	3.37	*0.36*					0.36	*0.1*			-2.24	*0.1*
A1	10	0.26	*0.03*	0.19	*0.04*	3.89	*0.26*					0.59	*0.07*			-2.26	*0.06*
A4	11	0.43	*0.09*	0.21	*0.03*	3.68	*0.25*					0.67	*0.04*			-2.13	*0.07*
A2	25	0.54	*0.14*	0	*0*	3.82	*0.29*					1	*0*			-2.2	*0.12*
A6	10	0.4	*0.04*	0	*0*	4.12	*0.5*					1	*0*			-2.28	*0.08*
A7	12	0.46	*0.03*	0.16	*0.01*	3.84	*0.1*					0.75	*0.02*			-2.13	*0.03*
A8	12	0.43	*0.03*	0.16	*0.01*	3.82	*0.11*					0.73	*0.02*			-2.14	*0.03*
A9	12	0.49	*0.03*	0.14	*0.01*	3.81	*0.11*					0.78	*0.02*			-2.12	*0.02*
A10	15	0.49	*0.02*	0.12	*0.01*	3.79	*0.1*					0.8	*0.01*			-2.13	*0.02*
Nb1	18	0	*0*	0.49	*0.03*	2.65	*0.09*	0.43	*0.06*			0.02	*0.02*	0.79	*0.02*	-2.28	*0.04*
Nb2	17	0.56	*0.05*	0.04	*0.03*	2.8	*0.09*	0.39	*0.08*			0.93	*0.05*	0.81	*0.03*	-2.18	*0.04*
Nb6	17	0.55	*0.05*	0.1	*0.03*	3.04	*0.11*	0.4	*0.07*			0.84	*0.04*	0.82	*0.02*	-2.12	*0.05*
Nb5	15	0.51	*0.05*	0.17	*0.04*	3.06	*0.07*	0.47	*0.06*			0.76	*0.05*	0.8	*0.02*	-2.08	*0.03*
Nb7	18	0.49	*0.04*	0.14	*0.04*	3.14	*0.07*	0.39	*0.05*			0.78	*0.05*	0.83	*0.02*	-2.12	*0.04*
Nb4	18	0.41	*0.05*	0.2	*0.03*	2.98	*0.09*	0.45	*0.07*			0.67	*0.05*	0.8	*0.02*	-2.14	*0.04*
Nb3	18	0.31	*0.03*	0.29	*0.03*	2.95	*0.1*	0.49	*0.08*			0.52	*0.04*	0.78	*0.02*	-2.15	*0.04*
B2	18	0.28	*0.03*	0.1	*0.02*	2.28	*0.27*					0.73	*0.04*			-2.56	*0.08*
B8	10	0.31	*0.05*	0.09	*0.03*	2.29	*0.31*					0.77	*0.06*			-2.54	*0.11*
B7	14	0.31	*0.04*	0.1	*0.05*	2.48	*0.4*					0.77	*0.09*			-2.51	*0.13*
B9	7	0.33	*0.07*	0.1	*0.03*	2.67	*0.48*					0.77	*0.05*			-2.46	*0.18*
B5	13	0.3	*0.04*	0.11	*0.02*	2.37	*0.2*					0.73	*0.03*			-2.51	*0.07*
B1	10	0.25	*0.02*	0.15	*0.02*	2.34	*0.22*					0.64	*0.04*			-2.53	*0.06*
B4	14	0.2	*0.04*	0.19	*0.03*	2.3	*0.39*					0.52	*0.06*			-2.55	*0.12*
B3	15	0.11	*0.03*	0.26	*0.04*	2.23	*0.33*					0.3	*0.06*			-2.59	*0.13*
B6	10	0	*0*	0.21	*0.04*	2.16	*0.57*					0	*0*			-2.86	*0.14*
B10	3	0.4	*0.01*	0	*0*	2.09	*0.22*					1	*0*			-2.58	*0.04*
S5	20	0.22	*0.01*	0.06	*0.02*	1.16	*0.09*					0.80	*0.04*			-3.09	*0.04*
T7 – 0.5kb	36	0.17	*0.02*	0.04	*0.01*	0.93	*0.03*					0.83	*0.04*			-3.20	*0.03*
S6	18	0.24	*0.02*	0.06	*0.02*	1.20	*0.19*					0.79	*0.03*			-2.95	*0.09*
S3b – QFM+4	21	0.21	*0.02*	0.07	*0.01*	1.24	*0.14*					0.75	*0.03*			-2.77	*0.03*
Nb9	20	0.16	*0.01*	0.11	*0.01*	0.97	*0.04*	0.14	*0.03*			0.61	*0.03*	0.81	*0.04*	-2.99	*0.04*
Nb11 – 0.5kb	25	0.13	*0.02*	0.09	*0.02*	0.64	*0.03*	0.10	*0.05*			0.58	*0.06*	0.86	*0.10*	-3.29	*0.08*
Nb16 – Ti	12	0.19	*0.06*	0.09	*0.02*	0.89	*0.20*	0.10	*0.06*	0.11	*0.07*	0.68	*0.07*	0.86	*0.10*	-3.06	*0.16*
Nb8	19	0.13	*0.01*	0.14	*0.02*	0.92	*0.07*	0.18	*0.04*			0.49	*0.04*	0.76	*0.04*	-2.98	*0.05*
Nb8b – QFM+4	33	0.12	*0.01*	0.13	*0.02*	1.06	*0.06*	0.11	*0.03*			0.47	*0.03*	0.86	*0.03*	-3.02	*0.05*
Nb13 – 0.5kb	21	0.10	*0.03*	0.12	*0.01*	0.56	*0.04*	0.11	*0.05*			0.46	*0.08*	0.80	*0.12*	-3.32	*0.07*
Nb14 - Ti	10	0.07	*0.03*	0.10	*0.06*	0.57	*0.08*	0.12	*0.05*	0.06	*0.02*	0.42	*0.16*	0.75	*0.06*	-3.41	*0.23*
Nb10	19	0.09	*0.01*	0.17	*0.01*	0.79	*0.06*	0.20	*0.02*			0.36	*0.04*	0.70	*0.03*	-3.04	*0.05*
Nb10b – QFM+4	40	0.08	*0.01*	0.13	*0.02*	0.95	*0.09*	0.16	*0.03*			0.39	*0.04*	0.79	*0.03*	-3.10	*0.07*
Nb12 – 0.5kb	21	0.07	*0.03*	0.14	*0.01*	0.55	*0.03*	0.12	*0.06*			0.33	*0.08*	0.81	*0.14*	-3.36	*0.08*
Nb15 – Ti	10	0.1	*0.04*	0.14	*0.06*	0.59	*0.17*	0.17	*0.07*	0.1	*0.07*	0.42	*0.13*	0.69	*0.08*	-3.22	*0.20*
Nb17 – 0.5kb	36	0.04	*0.01*	0.16	*0.02*	0.48	*0.03*	0.16	*0.05*			0.21	*0.04*	0.64	*0.06*	-3.33	*0.08*
Nb19	46	0.05	*0.01*	0.17	*0.01*	0.53	*0.04*	0.19	*0.04*			0.22	*0.04*	0.64	*0.05*	-3.24	*0.05*

n = number of analyses - *SD* = 2-sigma standard deviation on *n* analyses

Ksp = solubility product [(FeOxMnO)x(Ta_2O_5xNb_2O_5)]

Table 4. EPMA (conventional and FEG) compositions and structural formulae of experimental tantalite (Tant) and tapiolite (Tap)

		wt%						structural formula for 6O									
		FeO	MnO	Nb_2O_5	Ta_2O_5	TiO_2	Total	Fe^{3+}	Fe^{2+}	Mn	Nb	Ta	Ti	site A	site B	Total	Mn*	Ta*
800°C – FEG EPMA																		
S5	Tant	1.35	13.84		85.93		101.14		0.10	0.99		1.97		1.08	1.97	3.05	0.91	
N = 10		*0.17*	*0.46*		*1.47*		*1.88*										*0.01*	
S5	Tap	6.91	8.23		86.04		101.19		0.49	0.59		1.97		1.07	1.97	3.04	0.55	
N = 2		*0.14*	*0.48*		*0.29*		*0.33*										*0.01*	
T7-50MPa	Tant	0.24	16.07	1.71	81.10		99.12		0.02	1.15	0.07	1.87		1.17	1.93	3.10	0.99	0.97
N = 26		*0.29*	*0.66*	*1.79*	*2.00*		*1.00*										*0.02*	*0.03*
T7-50MPa	Tap	5.84	10.17	0.00	83.45		99.46		0.42	0.74	0.00	1.94		1.15	1.94	3.09	0.64	
N = 1		-	-	-	-		-										-	
S6	Tap	6.82	8.22		84.34		99.40		0.49	0.60		1.97		1.09	1.97	3.05	0.55	
N = 8		*0.37*	*0.33*		*2.00*		*1.76*										*0.02*	
S3b-QFM+4	Tant	3.67	12.29	0.01	83.48		99.46		0.26	0.89		1.94		1.15	1.94	3.09	0.77	
N = 20		*0.73*	*1.00*	*0.02*	*0.83*		*0.97*										*0.05*	
Nb9	Tant	4.99	10.55	14.60	68.13		98.27		0.33	0.71	0.52	1.46		1.04	1.99	3.02	0.68	0.74
N = 7		*0.31*	*0.75*	*1.45*	*1.74*		*0.53*										*0.03*	*0.02*
Nb11-50MPa	Tant	3.37	14.07	12.91	67.26		97.62		0.23	0.95	0.47	1.46		1.18	1.93	3.11	0.81	0.76
N = 36		*0.55*	*0.71*	*3.86*	*4.07*		*1.06*										*0.03*	*0.06*
Nb11-50MPa	Tap	10.01	6.27	1.14	80.01		97.44		0.72	0.46	0.04	1.88		1.18	1.93	3.11	0.38	0.98
N = 16		*0.38*	*0.88*	*1.10*	*1.27*		*0.99*										*0.02*	*0.02*
Nb16-Ti	Tap	10.13	5.53	3.91	79.00	2.46	101.02		0.68	0.38	0.14	1.72	0.15	1.10	1.96	3.06	0.35	0.92
N = 8		*0.27*	*0.69*	*1.73*	*2.66*	*1.03*	*2.03*										*0.03*	*0.03*
Nb16-Ti	Tant	4.22	11.19	9.04	74.53	2.76	101.73		0.27	0.73	0.31	1.56	0.16	1.05	1.98	3.03	0.75	0.83
N = 5		*0.57*	*1.24*	*3.45*	*3.69*	*1.11*	*1.45*										*0.02*	*0.06*
Nb8	Tant	7.36	10.02	18.74	64.64		100.76		0.46	0.64	0.64	1.32		1.10	1.96	3.06	0.58	0.68
N = 35		*0.62*	*1.48*	*2.15*	*2.43*		*1.62*										*0.05*	*0.03*
Nb8	Tap	10.92	3.31	7.81	74.70		96.74		0.77	0.23	0.30	1.70		1.00	2.00	3.00	0.23	0.85
N = 1		-	-	-	-		-		-	-	-	-		-	-	-	-	-
Nb8b-QFM+4		8.84	10.15	10.19	70.81		100.00	0.15	0.43	0.67	0.36	1.51		1.25	1.87	3.12	0.55	0.81
N = 31		*4.33*	*3.10*	*3.97*	*3.83*		*1.30*										*0.19*	*0.07*
Nb13-50MPa	Tant	5.95	12.17	15.16	64.65		97.93		0.39	0.81	0.54	1.38		1.20	1.92	3.12	0.67	0.72
N = 12		*0.42*	*0.54*	*0.99*	*1.33*		*1.06*										*0.02*	*0.02*
Nb13-50MPa	Tap	11.22	4.19	1.47	79.92		96.81		0.82	0.31	0.06	1.89		1.13	1.95	3.08	0.27	0.97
N = 17		*0.30*	*0.32*	*1.39*	*2.04*		*0.82*										*0.01*	*0.02*
Nb14-Ti	Tant	6.79	10.29	17.70	65.40	1.78	101.95		0.42	0.64	0.59	1.31	0.10	1.09	1.96	3.06	0.61	0.69
N = 10		*0.36*	*0.49*	*3.01*	*3.75*	*0.41*	*1.36*										*0.02*	*0.05*
Nb14-Ti	Tap	11.78	3.73	7.67	73.19	4.92	101.29		0.75	0.24	0.26	1.52	0.28	1.08	1.97	3.05	0.24	0.85
N = 14		*0.40*	*0.39*	*1.41*	*2.47*	*1.04*	*1.85*										*0.02*	*0.03*
Nb10	Tap	12.47	2.70	8.83	74.67		98.66		0.85	0.19	0.33	1.66		1.04	1.98	3.02	0.18	0.84
N = 11		*0.53*	*0.35*	*2.05*	*2.38*		*0.96*										*0.02*	*0.04*
Nb10	Tant	10.07	8.47	22.01	60.47		101.06		0.62	0.53	0.73	1.21		1.15	1.94	3.09	0.46	0.62
N = 12		*0.19*	*0.86*	*0.90*	*1.24*		*0.82*											
Nb10b-QFM+4	Tap	17.83	4.08	12.12	64.31		98.34	0.47	0.65	0.28	0.42	1.33		1.40	1.75	3.14	0.20	0.76
N = 16		*0.63*	*0.32*	*0.76*	*1.00*		*1.08*										*0.01*	*0.01*
Nb10b-QFM+4	Tant	10.09	9.39	19.82	62.14		101.44		0.62	0.59	0.66	1.25		1.21	1.91	3.13	0.49	0.65
N = 1		-	-	-	-	-	-										-	-
Nb12-50MPa	Tant	9.49	9.68	27.67	52.61		99.44		0.57	0.59	0.90	1.03		1.16	1.93	3.10	0.51	0.54
N = 15		*0.56*	*0.70*	*9.63*	*9.99*		*1.43*										*0.02*	*0.12*
Nb12-50MPa	Tap	13.13	2.81	4.61	76.88		97.43		0.93	0.20	0.18	1.77		1.13	1.95	3.08	0.18	0.91
N = 14		*0.40*	*0.40*	*2.76*	*3.31*		*0.83*										*0.02*	*0.05*
Nb15-Ti	Tap	12.51	2.48	8.90	70.69	5.86	100.45		0.79	0.16	0.30	1.45	0.33	1.06	1.98	3.04	0.17	0.83
N = 13		*0.45*	*0.27*	*0.65*	*1.44*	*1.58*	*1.71*										*0.02*	*0.01*
Nb17-50MPa	Tant	12.25	7.46	32.32	48.87		100.90		0.71	0.44	1.02	0.92		1.15	1.94	3.09	0.38	0.48
N = 45		*0.52*	*0.82*	*7.53*	*7.80*		*1.12*										*0.03*	*0.09*
Nb17-50MPa	Tap	15.08	1.51	9.95	72.19		98.72		1.02	0.10	0.36	1.59		1.12	1.95	3.07	0.09	0.82

N = 3		*0.53*	*0.11*	*6.68*	*8.44*	*1.44*								*0.01*	*0.12*
Nb19	Tant	12.90	6.58	31.16	50.66	101.30	0.75	0.39	0.98	0.96	1.14	1.94	3.08	0.34	0.50
N = 17		*0.43*	*0.63*	*6.65*	*7.38*	*1.03*								*0.02*	*0.08*

900°C – conventional EPMA

B2	Tant	1.24	11.66	88.40	101.30	0.09	0.83	2.03	0.92	2.03	2.95	0.90
N = 12		*0.25*	*0.28*	*0.55*	*0.58*							*0.02*
B8	Tant	1.48	11.93	88.01	101.42	0.10	0.85	2.02	0.96	2.02	2.97	0.89
N = 17		*0.14*	*0.26*	*0.37*	*0.43*							*0.01*
B7	Tant	1.65	11.63	87.35	100.45	0.12	0.84	2.02	0.95	2.02	2.97	0.88
N = 16		*0.08*	*0.16*	*0.50*	*0.55*							*0.00*
B7	Tap	5.30	7.45	87.76	100.45	0.38	0.54	2.03	0.92	2.03	2.95	0.59
N = 7		*0.11*	*0.16*	*0.79*	*0.90*							*0.01*
B9	Tant	5.09	7.87	88.26	101.21	0.36	0.56	2.03	0.92	2.03	2.95	0.61
N = 17		*0.12*	*0.09*	*0.69*	*0.68*							*0.01*
B5	Tap	5.76	6.86	88.30	100.92	0.41	0.49	2.04	0.90	2.04	2.94	0.55
N = 10		*0.17*	*0.14*	*0.93*	*0.87*							*0.01*
B1	Tap	6.95	5.67	88.36	100.98	0.49	0.41	2.04	0.90	2.04	2.94	0.45
N = 13		*0.13*	*0.11*	*0.84*	*0.82*							*0.01*
B4	Tap	8.39	4.36	88.46	101.22	0.59	0.31	2.04	0.91	2.04	2.94	0.35
N = 12		*0.30*	*0.11*	*0.67*	*0.69*							*0.01*
B3	Tap	10.53	2.11	88.27	100.91	0.75	0.15	2.04	0.90	2.04	2.94	0.17
N = 12		*0.16*	*0.09*	*0.93*	*0.97*							*0.01*
B6	Tap	12.68	0.00	88.04	100.73	0.90	0.00	2.04	0.90	2.04	2.94	0.00
N = 16		*0.28*	*0.00*	*0.87*	*0.90*							*0.00*
B10	Tant	0.05	13.11	87.94	101.10	0.00	0.94	2.02	0.94	2.02	2.97	1.00
N = 6		*0.06*	*0.17*	*0.95*	*1.03*							*0.00*

Table 4. *continued*

		wt%					structural formula for 6O								
		FeO	MnO	Nb_2O_5	Ta_2O_5	Total	Fe^{2+}	Mn	Nb	Ta	site A	site B	Total	Mn*	Ta*
						1000°C – conventional EPMA									
A5	Tap	12.28	0.00		87.89	100.22	0.88	0.00		2.05	0.88	2.05	2.93	0.00	
N = 5		*0.45*	*0.00*		*1.15*	*0.83*								*0.00*	
A3	Tap	10.23	2.17		88.09	100.49	0.73	0.16		2.05	0.89	2.05	2.93	0.18	
N = 9		*0.25*	*0.12*		*0.77*	*0.84*								*0.01*	
A1	Tap	7.35	5.24		88.47	101.07	0.52	0.38		2.04	0.90	2.04	2.94	0.42	
N=14		*0.15*	*0.11*		*0.46*	*0.49*								*0.01*	
A4	Tap	5.90	6.09		88.27	100.26	0.42	0.44		2.05	0.86	2.05	2.92	0.51	
N = 9		*0.16*	*0.20*		*0.68*	*0.79*								*0.01*	
A2	Tant	0.25	12.52		88.09	100.86	0.02	0.90		2.03	0.92	2.03	2.95	0.98	
N = 9		*0.07*	*0.25*		*0.57*	*0.65*								*0.01*	
A6	Tant	0.00	13.07		88.10	101.17	0.00	0.94		2.03	0.94	2.03	2.96	1.00	
N = 8			*0.21*		*0.76*	*0.69*								*0.00*	
A7	Tap	5.41	7.45		84.49	97.45	0.40	0.55		2.02	0.95	2.02	2.97	0.58	
N = 14		*0.12*	*0.19*		*0.56*	*0.63*								*0.01*	
A8	Tap	5.60	7.34		86.04	99.09	0.41	0.54		2.02	0.94	2.02	2.97	0.57	
N = 12		*0.17*	*0.16*		*1.21*	*1.11*								*0.01*	
A9	Tap	4.80	7.92		86.17	99.00	0.35	0.58		2.03	0.93	2.03	2.96	0.63	
N = 19		*0.17*	*0.25*		*1.55*	*1.48*								*0.01*	
A10	Tap	4.47	8.12		85.30	97.98	0.33	0.60		2.03	0.93	2.03	2.96	0.65	
N = 32		*0.11*	*0.26*		*0.71*	*0.70*								*0.01*	
A10	Tant	1.69	11.75		85.23	98.71	0.12	0.86		2.01	0.98	2.01	2.99	0.88	
N = 4		*0.07*	*0.31*		*0.75*	*0.51*								*0.01*	
Nb1	Tap	13.22	0.04	6.56	79.18	99.00	0.92	0.00	0.25	1.79	0.92	2.03	2.95	0.00	0.88
N = 13		*0.18*	*0.04*	*0.46*	*0.80*	*0.68*								*0.00*	*0.01*
Nb2	Tant	0.62	13.77	13.28	72.24	99.90	0.04	0.92	0.47	1.55	0.96	2.02	2.97	0.96	0.77
N = 10		*0.05*	*0.25*	*1.08*	*1.01*	*0.74*								*0.00*	*0.02*
Nb6	Tant	1.38	12.90	11.74	73.36	99.38	0.09	0.87	0.42	1.59	0.96	2.01	2.98	0.90	0.79
N = 8		*0.07*	*0.32*	*0.96*	*1.14*	*0.59*								*0.01*	*0.02*
Nb5	Tant	2.24	12.15	12.50	72.68	99.57	0.15	0.82	0.45	1.57	0.96	2.01	2.98	0.85	0.78
N = 14		*0.09*	*0.17*	*0.49*	*1.03*	*1.11*								*0.01*	*0.01*
Nb7	Tant	2.30	11.83	11.09	74.34	99.57	0.15	0.80	0.40	1.62	0.96	2.02	2.97	0.84	0.80
N = 7		*0.11*	*0.21*	*0.25*	*0.47*	*0.69*								*0.01*	*0.00*
Nb4	Tant	3.27	11.09	12.56	72.89	99.81	0.22	0.74	0.45	1.57	0.96	2.02	2.98	0.77	0.78
N = 21		*0.14*	*0.28*	*0.59*	*0.53*	*0.70*								*0.01*	*0.01*
Nb3	Tant	5.41	9.06	14.03	71.15	99.66	0.36	0.60	0.50	1.52	0.96	2.02	2.97	0.63	0.75
N = 7		*0.16*	*0.22*	*0.61*	*0.26*	*0.72*								*0.01*	*0.01*
Nb3	Tap	9.02	4.02	6.27	79.34	98.65	0.63	0.28	0.24	1.80	0.91	2.03	2.95	0.31	0.88
N = 32		*0.16*	*0.10*	*0.25*	*0.38*	*0.36*								*0.01*	*0.00*

N = number of analyses on which standard deviations were calculated